Acta Pharmaceutica Sinica B 2024;14(7):3232–3250

Chinese Pharmaceutical Association
Institute of Materia Medica, Chinese Academy of Medical Sciences

Acta Pharmaceutica Sinica B

www.elsevier.com/locate/apsb
www.sciencedirect.com

ORIGINAL ARTICLE

# A novel marine-derived anti-acute kidney injury agent targeting peroxiredoxin 1 and its nanodelivery strategy based on ADME optimization

**Ping Yu[a,†], Tanwei Gu[a,†], Yueyang Rao[b,c], Weimin Liang[a], Xi Zhang[a], Huanguo Jiang[a,c], Jindi Lu[a], Jianglian She[b], Jianmin Guo[d], Wei Yang[d], Yonghong Liu[b], Yingfeng Tu[a,*], Lan Tang[a,c,*], Xuefeng Zhou[b,c,*]**

[a]*Guangdong Provincial Key Laboratory of New Drug Screening, Guangdong-Hong Kong-Macao Joint Laboratory for New Drug Screening, School of Pharmaceutical Sciences, Southern Medical University, Guangzhou 510515, China*
[b]*CAS Key Laboratory of Tropical Marine Bio-Resources and Ecology, Guangdong Key Laboratory of Marine Materia Medica, South China Sea Institute of Oceanology, Chinese Academy of Sciences, Guangzhou 510301, China*
[c]*NMPA Key Laboratory for Research and Evaluation of Drug Metabolism, School of Pharmaceutical Sciences, Southern Medical University, Guangzhou 510515, China*
[d]*Guangdong Lewwin Pharmaceutical Research Institute Co., Ltd., Guangdong Provincial Key Laboratory of Drug Non-Clinical Evaluation and Research, Guangdong Engineering Research Center for Innovative Drug Evaluation and Research, Guangzhou 510990, China*

Received 17 November 2023; received in revised form 28 January 2024; accepted 7 February 2024

**KEY WORDS**

Acute kidney injury;
Piericidin glycoside;
Peroxiredoxin 1;
Nanodrug;

**Abstract** Insufficient therapeutic strategies for acute kidney injury (AKI) necessitate precision therapy targeting its pathogenesis. This study reveals the new mechanism of the marine-derived anti-AKI agent, piericidin glycoside S14, targeting peroxiredoxin 1 (PRDX1). By binding to Cys83 of PRDX1 and augmenting its peroxidase activity, S14 alleviates kidney injury efficiently in *Prdx1*-overexpression (*Prdx1*-OE) mice. Besides, S14 also increases PRDX1 nuclear translocation and directly activates

*Corresponding authors.
E-mail addresses: tuyingfeng1@smu.edu.cn (Yingfeng Tu), tl405@smu.edu.cn (Lan Tang), xfzhou@scsio.ac.cn (Xuefeng Zhou).
[†]These authors made equal contributions to this work.
Peer review under the responsibility of Chinese Pharmaceutical Association and Institute of Materia Medica, Chinese Academy of Medical Sciences.

https://doi.org/10.1016/j.apsb.2024.03.005
2211-3835 © 2024 The Authors. Published by Elsevier B.V. on behalf of Chinese Pharmaceutical Association and Institute of Materia Medica, Chinese Academy of Medical Sciences. This is an open access article under the CC BY-NC-ND license (http://creativecommons.org/licenses/by-nc-nd/4.0/).

Kim-1 targeted;
ADME;
Marine drug;
Druggability

the Nrf2/HO-1/NQO1 pathway to inhibit ROS production. Due to the limited druggability of S14 with low bioavailability (2.6%) and poor renal distribution, a pH-sensitive kidney-targeting dodecanamine-chitosan nanoparticle system is constructed to load S14 for precise treatment of AKI. L-Serine conjugation to chitosan imparts specificity to kidney injury molecule-1 (Kim-1)-overexpressed cells. The developed S14-nanodrug exhibits higher therapeutic efficiency by improving the *in vivo* behavior of S14 significantly. By encapsulation with micelles, the $AUC_{0-t}$, half-life time, and renal distribution of S14 increase 2.5-, 1.8-, and 3.1-fold, respectively. The main factors contributing to the improved druggability of S14 nanodrugs include the lower metabolic elimination rate and UDP-glycosyltransferase (UGT)-mediated biotransformation. In summary, this study identifies a new therapeutic target for the marine-derived anti-AKI agent while enhancing its ADME properties and druggability through nanotechnology, thereby driving advancements in marine drug development for AKI.

© 2024 The Authors. Published by Elsevier B.V. on behalf of Chinese Pharmaceutical Association and Institute of Materia Medica, Chinese Academy of Medical Sciences. This is an open access article under the CC BY-NC-ND license (http://creativecommons.org/licenses/by-nc-nd/4.0/).

## 1. Introduction

Acute kidney injury (AKI) is a clinical syndrome characterized by a rapid decline in renal function, resulting in elevated levels of serum creatinine and/or reduced urinary output[1]. Its occurrence is closely related to sepsis, renal ischemia−reperfusion injury and nephrotoxic drugs[2,3]. The pathophysiology of AKI remains incompletely understood, with a key role attributed to the injury and death of renal tubular cells, particularly those in the proximal tubule[4,5]. However, severe or sustained injury often leads to inadequate and incomplete repair, resulting in tubular degeneration, inflammation, renal fibrosis and ultimately progression to chronic kidney disease (CKD) or end-stage renal disease[6]. Currently, effective and targeted therapies for AKI are unavailable in the clinic, except for supportive management[7,8]. The Kidney Disease Improving Global Outcomes (KDIGO) guidelines for AKI recommend implementing various supportive measures in high-risk patients, including volume management, maintenance of adequate blood pressure, and judicious avoidance of nephrotoxins[9,10]. Therefore, effective therapeutic strategies are urgently needed based on the pathogenesis of AKI.

The piericidins are a family of microbial metabolites that feature a 4-pyridinol core linked with a methylated polyketide side chain. Piericidin A (PA) is a well-known mitochondrial complex I inhibitor and has garnered significant interest among medicinal chemists[11-13]. Previously, we have obtained 43 natural piericidins from two marine-derived *Streptomyces* strains[13-15], and several of them have shown promising potential in the treatment of renal cancer targeting peroxiredoxin 1 (PRDX1)[7]. Piericidin glycoside analogue 13-hydroxyglucopiericidin A (S14, Fig. 1A), could retard renal fibrosis and AKI by promoting autophagy and mitochondrial homeostasis as a novel liver kinase B1 (LKB1) activator[16]. In addition, S14 may also hold potential for AKI treatment through other crucial pathways. Subsequently, the ADME (absorption, distribution, metabolism, and excretion) study showed that the biotransformation of S14 within the body occurs rapidly (with a bioavailability of approximately 2.6%), by converting into S14-glucuronide and then excreting from the body, ultimately resulting in poor treatment efficiency (Supporting Information Fig. S1 and Table S1). Therefore, a strategy for precise AKI therapy may be achieved by improving the ADME characteristics of S14 by designing a certain kidney-targeted drug delivery system.

The pathogenesis of AKI is complicated and involves multiple mechanisms, including inflammation, oxidative stress, and vascular damage[17,18]. Among them, oxidative stress is considered the most prominent aggravating contributor[19]. Excessive production of reactive oxygen species (ROS) during AKI triggers mitochondrial cascades of inflammation, necrosis, and apoptosis[20]. Elevated levels of ROS have been shown to affect the physiology of kidney-associated cells, such as tubular endothelial cells, endothelial cells, and macrophages, prompting them to overexpress certain surface receptors, such as kidney injury molecule-1 (Kim-1), CD44, and E-selectin, etc. Kim-1, the first marker to be identified for AKI, is a transmembrane protein that is significantly up-regulated in the kidney during renal diseases, mainly expressed in the injured renal proximal tubules[21,22]. L-Serine, a potent renal tubular targeting modifier, also serves as a potential targeting agent for Kim-1[23]. Notably, polycationic carriers have shown significant potential in the delivery and treatment of AKI. Chitosan is a marine-derived natural cationic polysaccharide with excellent biocompatibility and biodegradability[24,25], making it a promising carrier for renal delivery[26,27]. L-Serine-modified chitosan (SC) was designed and used as an excellent Kim-1 targeted carrier for the precise treatment of AKI[28]. Furthermore, an ideal drug carrier should also release the drug to exert therapeutic effects in the injured renal cells (pH 6.5 of renal inflammation microenvironment, pH 4.5−5.0 of lysosomes)[29-32].

Here, a pH-sensitive Kim-1-targeted nanodrug was designed with enhanced delivery of marine-derived S14 and therapy for AKI. By combining dodecanamine (DA) with SC *via* an amide bond (pH-sensitive) to prepare SC-citraconic anhydride (CA)-DA amphiphilic polymer, the hydrophobic mitochondrial antioxidant S14 was efficiently loaded into the hydrophobic core of the micelles. S14-loaded nanodrugs realize AKI injured kidney targeting and pH-responsive releasing. We assessed the physicochemical properties, cellular uptake specificity, pH-responsive release, targeted biodistribution, and metabolism of the nanodrugs. Both *in vitro* and *in vivo* experiments were performed to evaluate the therapeutic potential of S14@SC-CA-DA for the prevention of AKI.

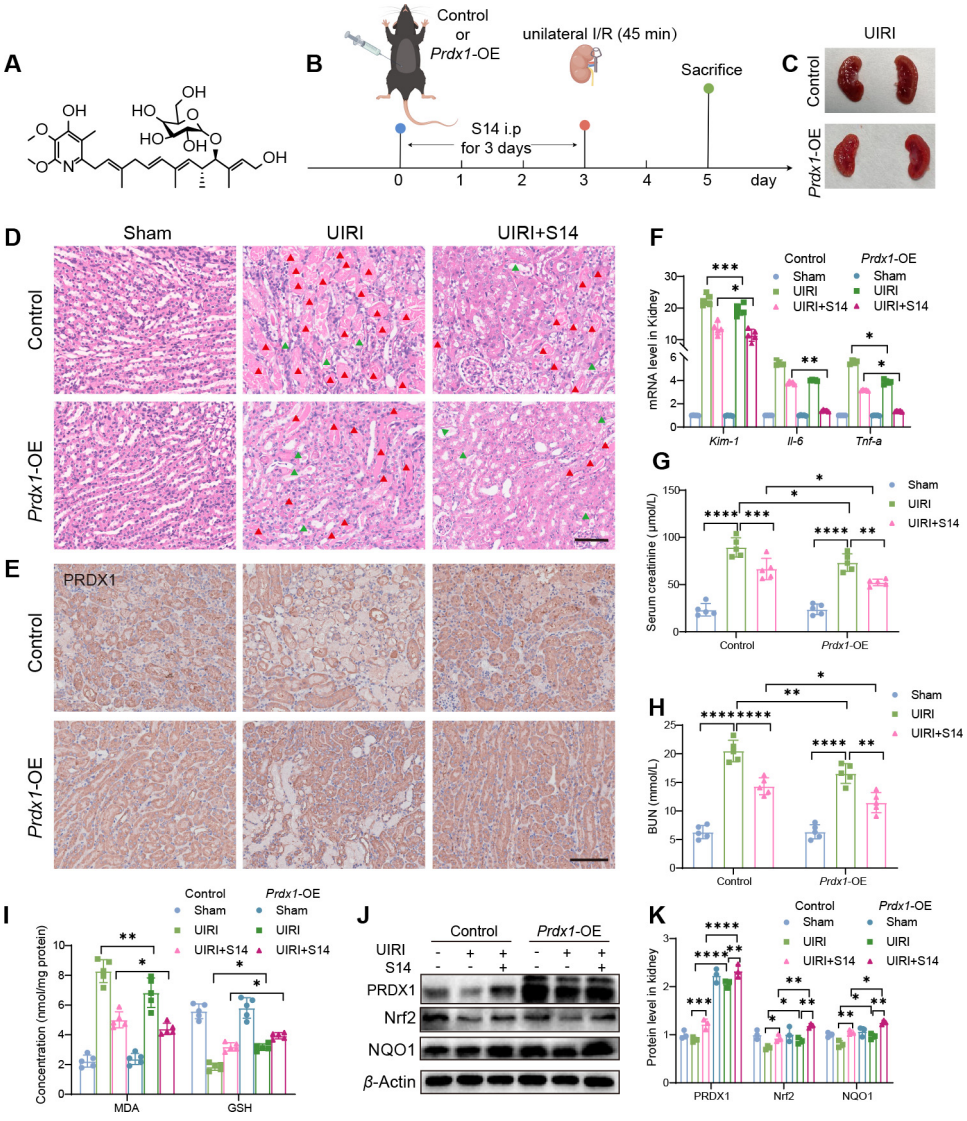


**Figure 1** PRDX1 overexpression attenuated AKI and S14 relieves renal function in UIRI mice *via* upregulating PRDX1. (A) Chemical structure of S14. (B) Scheme of S14 treatment. (C) Kidney photographs from Control and *Prdx1*-OE mice in the UIRI group. (D) H&E staining from Control and *Prdx1*-OE mice in the indicated groups (scale bar = 100 μm). (E) Immunohistochemistry for PRDX1 in kidney tissues (scale bar = 100 μm). (F) The mRNA expression of *Kim-1*, *Il-6*, and *Tnf-a* in the kidney from Control and *Prdx1*-OE mice in each group. Data are mean ± SD ($n = 5$). (G, H) Serum creatinine (Scr) and BUN levels from Control and *Prdx1*-OE mice in the indicated groups. Data are mean ± SD ($n = 5$). (I) MDA and GSH levels from Control and *Prdx1*-OE mice in the indicated groups. (J) Protein expression of PRDX1, Nrf2, and NQO1 in the kidney from Control and *Prdx1*-OE mice in the indicated groups. (K) Quantification of the protein immunoblots of PRDX1, Nrf2, and NQO1. Data are presented as mean ± SD ($n = 3$). *$P < 0.05$, **$P < 0.01$, ***$P < 0.001$ and ****$P < 0.0001$.

## 2. Materials and methods

### 2.1. *Materials*

Chitosan (MW ≈ 3 kDa, degree of deacetylation, DD > 90%) was purchased from Yuanye Biotechnology Co., Ltd. (Shanghai, China). Boc-L-Ser(tBu)-OH, citraconic anhydride, succinic, anhydride dodecylamine, pyrene, *O*-(*N*-succinimidyl)-*N*,*N*,*N*′,*N*′-tetramethyluronium tetrafluoroborate (TSTU), trifluoroacetic acid (TFA), triisopropo-pylsilane (TIS) and Pyrene were purchased from Macklin Biochemical Co., Ltd. (Shanghai, China). Serum creatinine and BUN kits were purchased from Nanjing Jiancheng Bioengineering Institute (Nanjing, China). 1,1′-Dioctadecyl-3,3,3′,3′-tetramethylindodicarbocyanine perchlorate (DiD), Hoechst 33258, mitochondrial membrane potential assay (JC-1) and MDA kits were purchased from Beyotime Biotechnology Co., Ltd. (Shanghai, China). TNF-α and IL-6 ELISA kits from Jiangsu Meimian Industrial Co., Ltd. (Yancheng, China). Mouse PRDX1 enzyme-linked immunosorbent assay kit from Enzyme-linked Biotechnology Co., Ltd. (Shanghai, China). The following primary antibodies were used: anti-Kim-1 (Novus Biologicals, NBP1-76701SS, USA), anti-PRDX1 (HuaBio, ET1702-08, China), anti-Nrf2 (ABclonal, A1244, China), anti-Nrf2 (Santa Cruze, SC365949, USA), anti-NQO1 (ABclonal, A23486, China), anti-HO-1 (ABclonal, A1346, China), anti-Bax antibody (ABclonal, A19684, China), anti-Bcl-2 (ABclonal, A0208,

China), anti-Lamin B1 (ABclonal, A11495, China), anti-Caspase-3 (Abmart, T40044, China), and anti-Caspase-9 (Abmart, T40046, China). The following secondary antibodies were used: HRP-conjugated secondary antibodies (Fude, China), and Alexa 488/549-conjugated secondary antibodies (Abmart, China). All other solvents were of analytical or chromatographic grade.

### 2.2. Animals

Male C57BL/6 mice (7−8 weeks old, 20−25 g) were purchased from the experimental animal center of Southern Medical University, *Prdx1*-OE mice were generated using the CRISPR/Cas9 system on a C57BL/6 background (Biomodel Organism Science & Technology Development Co., Ltd., Shanghai, China), and validated by PCR genotyping and expression profiling (Supporting Information Fig. S2 and Table S2). Animal experimental protocols gained approval by the Institutional Animal Care and Use Committee of Southern Medical University Experimental Animal Center.

### 2.3. Ischemia−reperfusion model of AKI

To induce AKI, we employed the unilateral ischemia−reperfusion (UIRI) technique in C57BL/6 mice. The left renal pedicles were clipped using microaneurysm clamps to induce renal ischemia. Throughout the ischemic period, we maintained the body temperature at approximately 37 °C using a temperature-controlled heating system. After 45 min, the clamps were released, reperfusion was visually confirmed, and wounds were sutured.

### 2.4. Immunofluorescence staining

For cell Immunofluorescence staining, the cells were fixed with acetone and subjected to gradient alcohol elution. Subsequently, they were blocked with a blocking buffer containing 1% BSA and 0.5% Tween 20 in PBS at room temperature for 1 h. Afterward, the HK-2 cells were incubated with primary antibodies overnight at 4 °C. Following this, the cells were incubated with Alexa Fluor 488/594-conjugated secondary antibodies and DAPI for 2 h at room temperature. For kidney tissue immunostaining, the kidney sections were fixed in 4% paraformaldehyde, eluted with gradient alcohol, permeabilized, and embedded. The kidney sections were incubated with primary antibody and then with secondary antibody Alexa Fluor 488-conjugated goat anti-Rabbit IgG and DAPI. Images were acquired using an Olympus FV3000 confocal laser microscope.

### 2.5. Immunoprecipitation assay

To perform the Immunoprecipitation assay, the plasmids Flag or Flag-PRDX1 were transfected into HK-2 cells using Lipofectamine 3000 reagent (Invitrogen, USA) following the provided protocol. After 48 h of transfection, the cells were harvested for Western blotting and immunoprecipitation analysis.

### 2.6. siRNA transfection

Transfection of HK-2 cells with *PRDX1* siRNA or negative control siRNA (Santa Cruz, USA) was performed using Lipofectamine 3000 (Invitrogen, USA), according to the manufacturer's instructions. The knockdown efficiency of PRDX1 was determined by immunoblot at 48 h post-transfection.

### 2.7. Surface plasmon resonance (SPR)

SPR measurements were conducted using the PlexArray HT A100 system (Plexera LLC, Bothell, WA, USA) to analyze the interaction. The immobilization of human PRDX1 protein (Cloud Clone, RPC749Hu01, China) was achieved on a nano-capture sensor chip with a bare gold coating. S14 was diluted in PBS buffer at concentrations of 0.3125−2.5 μmol/L and injected in the multicycle analysis mode. The data were analyzed using BIA evaluation Software.

### 2.8. Synthesis of SC-CA-DA and SC-DA

The pH-sensitive SC-CA-DA was synthesized using an amination reaction as follows. L-Serine−modified chitosan was synthesized by the previous report[21]. Boc-Ser(tBu)-OH (preSer) (456.94 mg, 1.75 mmol) and TSTU (530.44 mg, 1.75 mmol) were dissolved in 10 mL of anhydrous *N*,*N*′-dimethylformamide (DMF). After stirring for 15 min, *N*,*N*-diisopropylethylamine (DIPEA; 304 μL, 1.75 mmol) was added, and the resulting solution was stirred for 4 h. Subsequently, a solution of chitosan (3 kDa, 1.5 g, 500 μmol) in 10 mL of deionized water was added to the reaction mixture. The solution was stirred at room temperature for 12 h and then purified by dialysis [molecular weight cutoff (MWCO), 2.0 kDa] against deionized water for 2 days, followed by lyophilization.

The 4-(dodecylamino)-2-methyl-4-oxobut-2-enoic acid (CA-DA) compound was synthesized by the previous report[33]. Briefly, 10.2 mmol of the n-dodecylamine in 5 mL ethyl ether was added dropwise at 4 °C to the stirred citraconic anhydride (10 mmol) in ethyl ether (10 mL). The mixed solution was refluxed at 40 °C for 2 h, and the compound was obtained by filtration. The structure was confirmed by the $^{1}$H and $^{13}$C NMR spectra. Yield: 90%.

The preSC-CA-DA was synthesized by conjugating CA-DA to preSC. In short, CA-DA (148.72 mg, 0.5 mmol) was dissolved in 5 mL of DMF at room temperature and mixed with TSTU (165.33 mg, 0.55 mmol). After stirring the solution for 15 min, DIPEA (95 μL, 0.55 mmol) was added. Subsequently, a solution of preSC (1 g, 0.25 mmol) in 5 mL of deionized water was added. The mixture was stirred at room temperature for 24 h and then purified by dialysis (MWCO, 2 kDa) against deionized water for 2 days, followed by lyophilization. To deprotect the Boc and tBu groups, the products were dissolved in a TFA cocktail (95% TFA, 2.5% TIS, and 2.5% water). The reaction mixtures were incubated at room temperature for 30 min. Once deprotection was complete, the solution was evaporated to remove most of TFA. The residue was purified by dialysis (MWCO, 2.0 kDa) against deionized water for 2 days, followed by lyophilization.

The preparation method for non-pH sensitive SC-DA shared similarities with that of SC-CA-DA, except for replacing citraconic anhydride with succinic anhydride.

### 2.9. Preparation and characterization of micelles S14@SC-CA-DA and S14@SC-DA

S14-loaded micelles S14@SC-CA-DA and S14@SC-DA were prepared as follows: SC-CA-DA or SC-DA (5 mg) and S14 (0.4 mg) were dispersed in DMSO (200 μL). The mixture was then added dropwise into dd$H_2O$ (800 μL) while stirring for 12 h. Subsequently, the product was purified by dialysis (MWCO, 2.0 kDa) against deionized water for 12 h to remove the unentrapped S14. The particle size was determined using Dynamic Light Scattering (DLS; Malvern Instruments Co., Ltd., Zetasizer

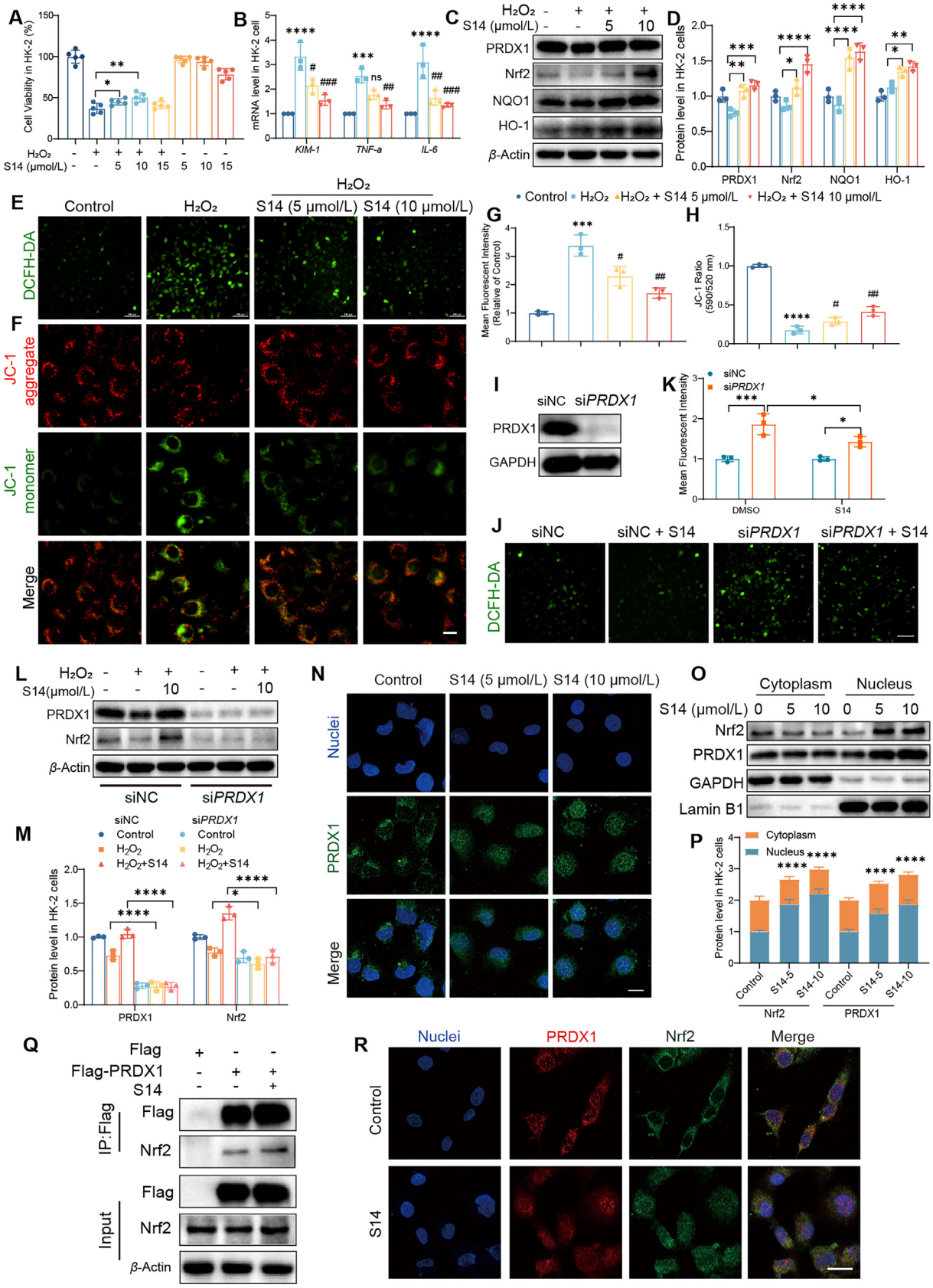


**Figure 2** S14 reduced $H_2O_2$-induced cell apoptosis through regulating PRDX1/Nrf2 in HK-2. (A) The viability of HK-2 cells after $H_2O_2$ treatment and treatment with or without S14. Data are presented as mean ± SD ($n = 5$) (B) The mRNA expression of KIM-1, IL-6, and TNF-a in HK-2 cells. Data are presented as mean ± SD ($n = 3$). (C) Representative Western blot results for PRDX1, Nrf2, NQO1, and HO-1 in HK-2 after

Nano ZSE, UK), and the morphology was examined using a Transmission Electron Microscope (TEM; JEOL-1400, Japan).

### 2.10. Mitochondrial structure observation

The kidney tissue was fixed with glutaraldehyde (2.5%), dehydrated in graded alcohols, and then subjected to osmotic embedding and sectioning. After staining, the kidney sections were observed by TEM (HITACHI, HT7700, Japan).

### 2.11. Pharmacokinetic assay

Male C57BL/6 mice ($n = 5$) were intravenously injected with S14 and S14@SC-CA-DA (S14-equivalent 2.0 mg/kg), respectively. Blood samples (50 μL blood per mouse) were collected in heparin-treated tubes at predetermined time points (2, 5, 15, 30, 60, 90, 120, and 150 min). The blood samples were then centrifuged at 4 °C (8000 rpm) for 10 min to obtain plasma (DLAB D3024R, Beijing, China). The content of S14 in plasma was detected by LC−MS/MS (SHIMADZU LC-30AD with AB SCIEX instruments 4000 Q-Trap, Japan). Pharmacokinetic parameters were calculated by DAS 2.0 software (Mathematical Pharmacology Professional Committee of China, Shanghai, China).

### 2.12. Determination of S14 concentration in major organs of AKI mice

The C57BL/6 mice subjected to unilateral renal IR were divided into the S14 group and the S14@SC-CA-DA group. The mice were euthanized after 30 and 150 min of injection of the aforementioned preparation at a dose of S14 (2 mg/kg), and the heart, liver, spleen, lung, and kidney were collected for drug detection. A 20% tissue homogenate (100 μL) was mixed with 400 μL testosterone internal standard solution (100 ng/mL), vortexed for 3 min, and then centrifuged at 13,000 rpm for 20 min (DLAB D3024R, Beijing, China). The supernatant was vacuum-dried overnight, and the residue was reconstituted with 100 μL of 50% acetonitrile aqueous solution. After centrifugation at 13,000 rpm for 20 min, the supernatant was injected into the LC−MS/MS analysis.

### 2.13. Statistical analysis

We utilized the Prism GraphPad software to perform all statistical analyses, including Student's *t*-test, one-way ANOVA, and two-way ANOVA; $^{*}P < 0.05$, $^{**}P < 0.01$, $^{***}P < 0.001$, $^{****}P < 0.0001$.

## 3. Results

### 3.1. PRDX1 overexpression attenuated AKI and S14 relieves renal function in UIRI mice via upregulating PRDX1

The protective effect of S14 against unilateral ischemia−reperfusion injury (UIRI)-induced AKI was investigated (Fig. 1A and B). Oxidative stress is a key mediator of tissue damage after ischemia−reperfusion[34,35]. PRDX1, an antioxidant enzyme, is capable of catalyzing the peroxide reduction[36,37]. Compared with Control mice, UIRI-induced kidney injury was significantly reduced in *Prdx1*-OE mice, supporting a critical role of PRDX1 in disease progression (Fig. 1C). Hematoxylin and eosin (H&E) staining showed that S14 markedly attenuated the UIRI-induced tubular epithelial cell necrosis and detachment in Control mice (Fig. 1D). Furthermore, UIRI and S14 treatment groups significantly attenuated kidney damage in *Prdx1*-OE mice compared with Control mice. Moreover, PRDX1 overexpression improved UIRI-induced kidney injury as evidenced by improved kidney function, reduced oxidative stress markers (MDA and GSH), decreased expression of kidney injury molecule-1 (*Kim-1*) and pro-inflammatory genes (*Tnf-α* and *Il-6*). Similarly, after treatment with S14, renal function was markedly relieved in *Prdx1*-OE UIRI mice compared with Control UIRI mice (Fig. 1F−I). Immunohistochemistry staining and immunoblot analysis confirmed that S14 significantly restored the expression of PRDX1, Nrf2 (cellular redox regulator), NQO1 and HO-1 proteins in UIRI mice (Fig. 1E and J−K). These results collectively indicate that S14 ameliorates renal function in UIRI mice by upregulating PRDX1.

### 3.2. S14 reduced $H_2O_2$-induced cell apoptosis through regulating PRDX1/Nrf2 in HK-2

To investigate the molecular mechanisms of S14 in HK-2 cells, it is crucial to clarify the relationship between PRDX1 and ROS levels. The cell counting kit-8 (CCK-8) assay indicated that S14 treatment had no significant cytotoxic effect on HK-2 cells with concentrations of 5−10 μmol/L. Oxidative stress was induced using $H_2O_2$, resulting in a decrease of over 50% in HK-2 cell viability after 24 h of exposure to 500 μmol/L $H_2O_2$. Nevertheless, the cytotoxic effect was markedly alleviated in the presence of S14 (5 and 10 μmol/L) in HK-2 cells (Fig. 2A). The mRNA levels of *KIM-1* and pro-inflammatory factors (*TNF-a* and *IL-6*) were reduced following S14 treatment compared to $H_2O_2$ treatment alone (Fig. 2B). The expression levels of PRDX1, Nrf2, and NQO1 proteins were observed to decrease upon exposure to $H_2O_2$-induced oxidative stress. However, in the $H_2O_2$ + S14 group, the protein levels of PRDX1, Nrf2, and NQO1 were maintained at a significantly higher level in HK-2 cells (Fig. 2C and D). Additionally,

$H_2O_2$ treatment and treatment with or without S14. (D) Quantification of the Western blot data from (C). (E) Fluorescence images of the DCFH-DA probe for hydrogen peroxide in HK-2 cells (scale bar = 100 μm). (F) Fluorescence images of JC-1 staining in HK-2 cells (scale bar = 20 μm). (G) The ROS mean fluorescence intensity of (E). (H) The mean ratio of fluorescence intensity of JC-1 aggregates and JC-1 monomers in (F). (I) Protein expression of PRDX1 in HK-2 cells was transiently transfected with PRDX1 siRNA (50 nmol/L) for 48 h. Data are presented as mean ± SD ($n = 3$). (J) The intracellular ROS detection in HK-2 cells was transiently transfected with PRDX1 siRNA, followed by treatment with S14 for another 24 h (scale bar = 100 μm). Data are mean ± SD ($n = 3$). (K) The ROS mean fluorescence intensity of (J). (L) Representative immunoblots results for Nrf2 and PRDX1 in HK-2 cells transfected with PRDX1-siRNA after $H_2O_2$ treatment and treatment with or without S14. (M) Quantification of the immunoblots data from (L). (N) Representative images for immunofluorescent staining of HK-2 treated with S14 after co-incubating for 24 h (scale bar = 20 μm). PRDX1 (green), nuclei (blue). Data are mean ± SD ($n = 3$) (O) Immunoblot analysis of PRDX1 protein in nuclear and cytosol extracts of HK-2 cells treated with S14. (P) Quantification of the immunoblots data from (O). (Q) Representative immunoprecipitation analysis of the binding of PRDX1 to Nrf2 in HK-2 and treatment with or without S14. (R) Confocal microscopy images of Nrf2 (green) and PRDX1 (red) (scale bar = 20 μm). Data are mean ± SD ($n = 3$). *P*-values are indicated as $^{*}P < 0.05$, $^{**}P < 0.01$, $^{***}P < 0.01$ and $^{****}P < 0.0001$. ns, not significant. $^{\#}P < 0.05$, $^{\#\#}P < 0.01$ and $^{\#\#\#}P < 0.001$ as compared with $H_2O_2$ group.

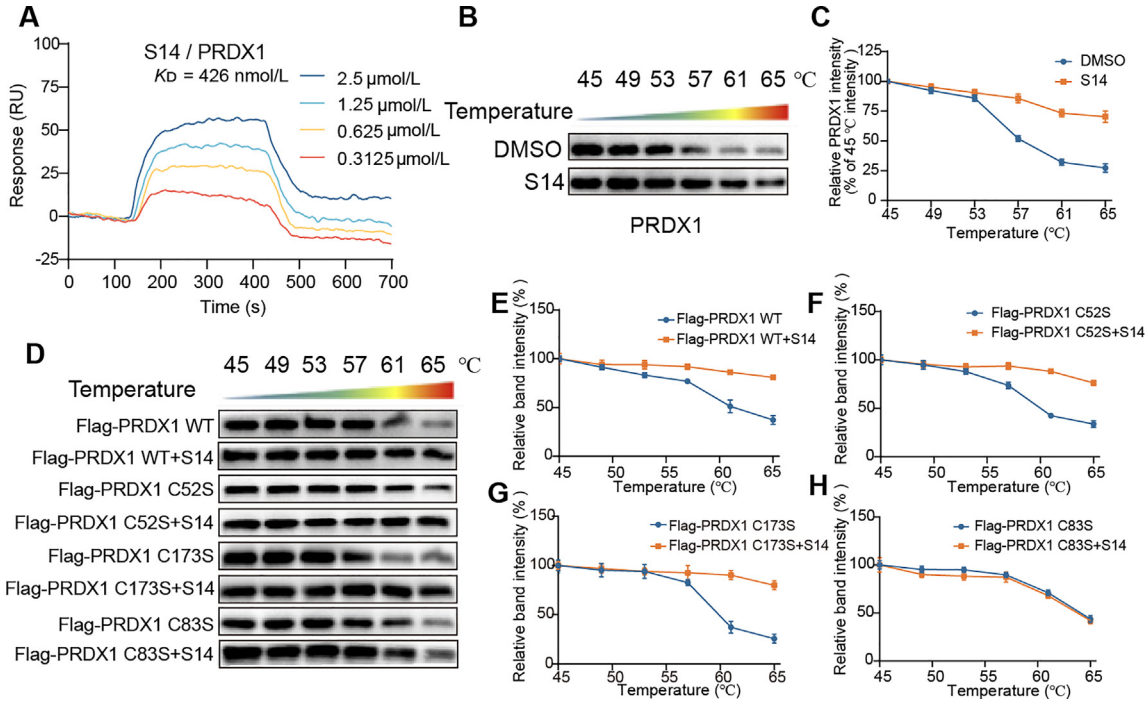


**Figure 3** S14 binds to the PRDX1 protein. (A) The affinity activities of S14 to PRDX1 protein were analyzed using the SPR assay. (B) Cellular thermal shift assay (CETSA)-Western blot to test the interactions of S14 and PRDX1. (C) The relative immunoblotting band density is analyzed. (D) Cellular thermal shift assay of WT PRDX1 or mutated PRDX1 in HK-2 cells treated with or without S14. (E−H) The relative immunoblotting band density is analyzed. Data are mean ± SD ($n$ = 3).

fluorescence analysis showed that S14 markedly reduced ROS levels and stabilized mitochondrial membrane potential (MMP) in $H_2O_2$-treated cells (Fig. 2E−H).

To further elucidate the mechanism by which PRDX1 inhibits oxidative stress. We used small interfering RNA (siRNA) to knock down *PRDX1* in HK-2 cells and speculate on the role of ROS (Fig. 2I). Knockdown of *PRDX1* resulted in elevated ROS levels compared to siNC HK-2 cells. However, treatment with S14 reduced ROS levels in si*PRDX1* HK-2 cells (Fig. 2J and K). Subsequently, we transfected si*PRDX1* into HK-2 cells under oxidative stress in the presence or absence of S14. Transfection with siRNA significantly reduced PRDX1 protein expression. And no significant difference was observed between the $H_2O_2$ group and $H_2O_2$ + S14 group. Furthermore, the expression level of Nrf2 was similarly suppressed in both groups, even after adding S14 (Fig. 2M).

PRDX1 not only acts as an antioxidant enzyme but also as a molecular chaperone, capable of modulating the actions of numerous molecules or as a transcriptional regulator[38,39]. PRDX1 can directly interact with nuclear transcriptional factors and modulate gene expression such as c-Myc and Nrf2[40]. Therefore, we further investigated the protein levels of PRDX1 and Nrf2 in the nucleus and cytosol of HK-2 cells. The results demonstrated that S14 promoted the translocation of PRDX1 and Nrf2 to the nucleus (Fig. 2N−P). To assess the binding between PRDX1 and Nrf2, immunoprecipitation, immunofluorescence and surface plasmon resonance experiments (SPR) indicated that PRDX1 was coupled with Nrf2 (Fig. 2Q and R, Supporting Information Fig. S3). Some studies have shown that promoting the entry of Nrf2 can regulate downstream heme oxygenase-1 (HO-1) expression to inhibit ROS production[41,42]. These findings collectively suggest that PRDX1 binds with nuclear transcriptional factors Nrf2 to regulate ROS levels.

### 3.3. *S14 directly binds to the PRDX1 protein*

S14 increased nuclear translocation and protein expression of PRDX1. Therefore, we further explored whether S14 could bind to PRDX1 by surface plasmon resonance and cellular thermal shift assay followed by Western blotting (CETSA-WB) assay. The SPR analysis demonstrated that S14 bound to human PRDX1 protein with dissociation equilibrium constants (KD) of 426 nmol/L (Fig. 3A). Additionally, the CETSA assay result indicated that S14 could markedly enhance the thermal stability of PRDX1 compared to the DMSO group, providing further support for the direct binding target of S14 to PRDX1 as its target (Fig. 3B and C). CETSA assay was used to assess the binding of small molecules to target proteins by evaluating the thermal stability of the target protein[43]. Moreover, to identify the drug binding site of S14 on the PRDX1 protein. Herein, we transfected HK-2 cells with plasmids encoding Flag-tagged wild-type PRDX1 (Flag-PRDX1 WT), or mutant PRDX1 with cysteine substitutions at positions 52 (Cys52S), 173 (Cys173S), or 83 (Cys83S) for two days. Subsequently, the cells were treated with DMSO or S14 for 4 h. The results indicated that S14 treatment did not elicit any changes in protein stabilization against thermal variations in cells transfected with Flag-PRDX1 C83S plasmid (Fig. 3D−H). These results suggest that S14 mainly binds to Cys83 of PRDX1 rather than Cys52 and Cys172 sites.

### 3.4. *Synthesis and characterization of SC-CA-DA and SC-DA*

We performed the synthesis of the pH-responsive SC-CA-DA conjugate targeted towards Kim-1 using CA as a linker between DA and SC (Supporting Information Fig. S4). Boc-L-Ser(tBu)-OH-modified chitosan (preSC) was prepared by constructing

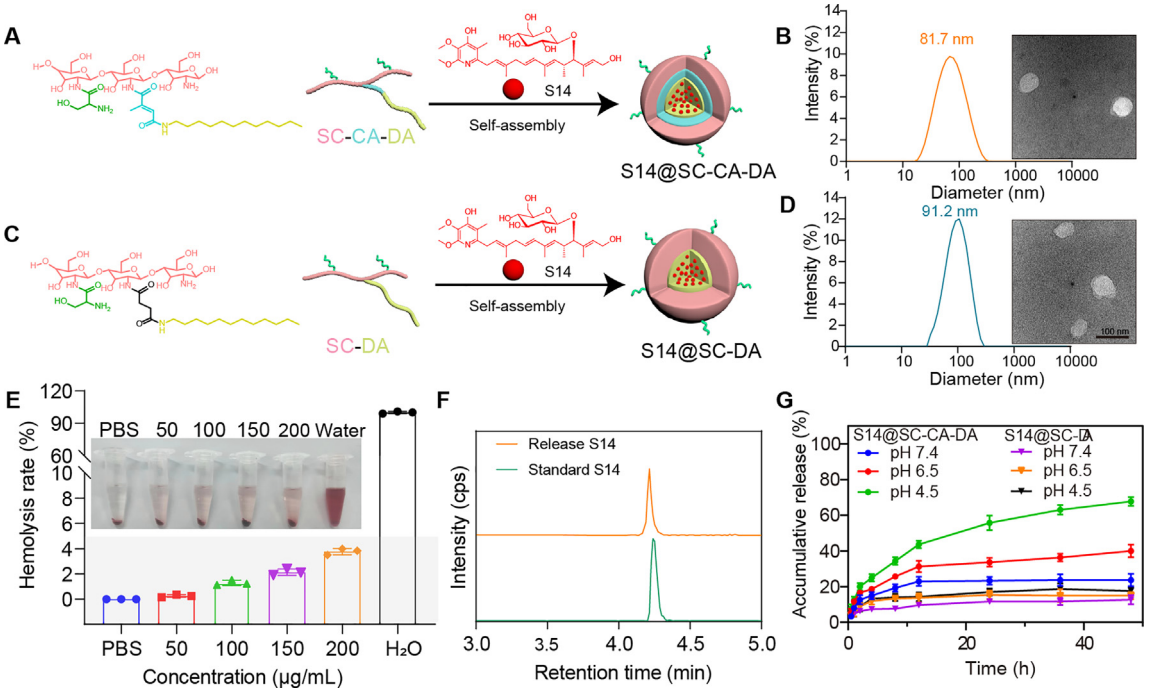


**Figure 4** Preparation and characterization of the micelles. (A) The preparation of S14@SC-CA-DA micelles. (B) Size distribution and TEM image of S14@SC-CA-DA micelles. (C) The preparation of S14@SC-DA micelles. (D) Size distribution and TEM image of S14@SC-DA micelles. (E) Relative hemolysis ratio of various concentrations of S14@SC-CA-DA micelles. (F) Absorption peaks of released S14 monitored by LC−MS/MS. (G) The release rates of S14 from S14@SC-CA-DA and S14@SC-DA micelles at different pH values. Data are mean ± SD ($n$ = 3).

Boc-L-Ser(tBu)-OH (preSer) on the amino group of chitosan. The chemical structure of preSC was analyzed by $^1$H nuclear magnetic resonance (NMR) spectrum (Supporting Information Fig. S5). It was found that preSC had the characteristic peaks of preSer at ∼1.1 and 1.4 parts per million (ppm), which belonged to the *tert*-butyl carbonyl (Boc) and *tert*-butyl (tBu) groups, respectively. According to the integrated area of the characteristic peaks, the substitution degree of Boc-L-Ser(tBu)-OH is 28%. Then, CA and DA were employed to synthesize the CA-DA ester, and the preSC-CA-DA conjugate was obtained by reacting the amino group of preSC with the carboxyl group of the CA-DA ester *via* carbon diamine, followed by trifluoroacetic acid (TFA) cocktail treatment to deprotection of Boc and tBu groups. Under acidic conditions, the double bond in the citrate amide promoted the internal attack of the amide carbonyl group by the carboxylate, thereby accelerating the cleavage of the amide bond[44]. Meanwhile, we also prepared a pH-insensitive SC-DA conjugate using succinic anhydride (SA) instead of CA as the linker between SC and DA in a similar process. The $^1$H NMR spectrum of SC-CA-DA exhibited characteristic peaks of DA (f 7.86 ppm), −$CH_3$ (e 0.85 ppm), the double bond (n 5.8 ppm), and −$CH_3$ (d 1.93 ppm) of citraconic acid ester, comparing with those of chitosan (Fig. S4). From the integrated area of the characteristic peaks, the degree of substitution of DA was similar for SC-DA and SC-CA-DA with 36.4% and 37.0%, respectively. Chitosan (C)-CA-DA was synthesized using the amidation reaction method. The $^1$H NMR spectrum showed the presence of characteristic peaks of DA in the spectra of C-CA-DA, demonstrating the successful synthesis of C-CA-DA.

### 3.5. *Preparation and characterization of micelles*

The polymer SC-CA-DA and SC-DA were self-assembled in an aqueous solution to prepare micelles (Supporting Information Table S4), the obtained micelles had similar particle size (∼100 nm) and potential (∼18 mV). In addition, the low critical micelle concentration (CMC) of SC-CA-DA (72.1 μg/mL) indicated that the micelles could resist hemodilution and remain stable at low concentrations (Supporting Information Fig. S6). S14, a hydrophobic drug lead (Supporting Information Fig. S7), was self-assembled with SC-DA and SC-CA-DA through hydrophobic interaction, respectively (Fig. 4A and C). The S14-loaded micelles were spherical with uniform size distribution. S14@SC-DA and S14@SC-CA-DA showed similar particle size (∼90 nm) and potential (about 20 mV) (Fig. 4B and D, Table S4). Remarkably, the size of the S14-loaded micelles was smaller than that of the blank micelles, possibly due to the interaction between S14 and hydrophobic fragment CA-DA. The encapsulation efficiency (EE%) of S14@SC-CA-DA was determined to be 80.2 ± 3.1%, with a drug-loading (DL%) capacity of 9.6 ± 2.5%. Furthermore, S14@SC-CA-DA exhibited favorable size stability in both PBS and 10% FBS (Supporting Information Fig. S8). The erythrocyte hemolysis rate of micelles remained below 5.0% in the range of 200 μg/mL (Fig. 4E), indicating good biological safety and compliance with the requirements of biomedical materials.

For the pH-responsive S14@SC-CA-DA nanodelivery system, the drug release rate increased significantly with decreasing pH value. The concentration of S14 was measured by LC−MS/MS, with good linearity ($R^2$ = 0.9976) and range (1−1000 ng/mL)

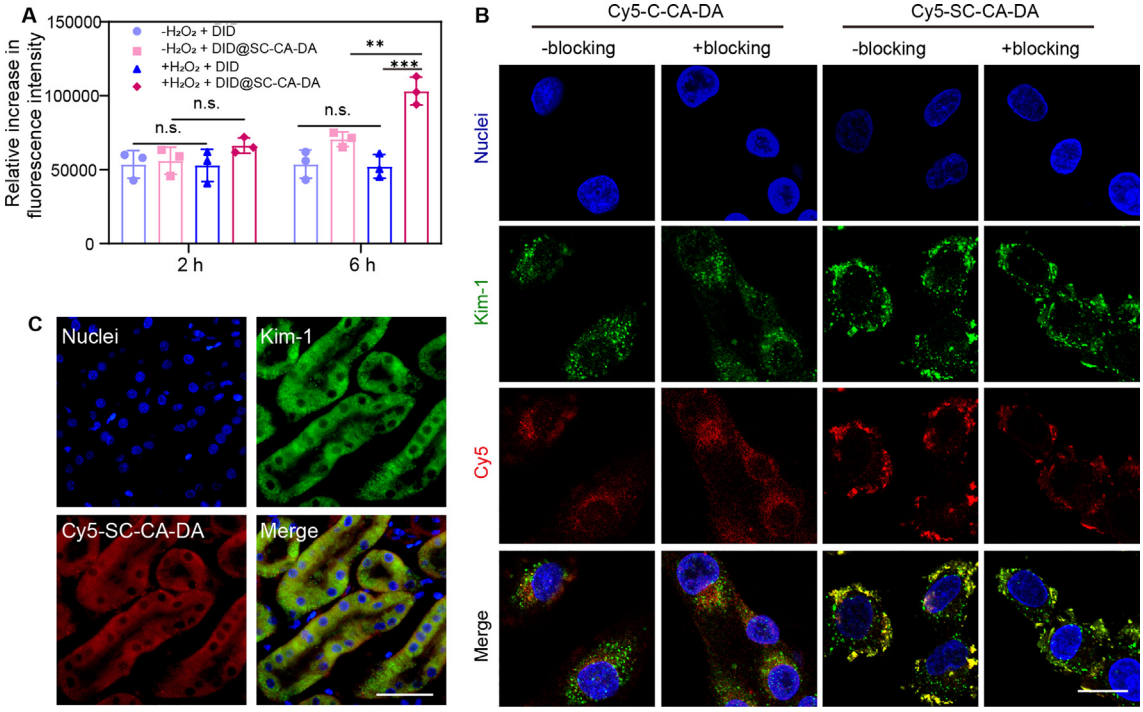


**Figure 5** Kim-1−associated endocytosis of SC-CA-DA *in vitro* and *in vivo*. (A) Fluorescence microscopic assay of micelles uptake by normal or $H_2O_2$-stimulated HK-2 cells for 2 or 6 h. The data are the means ± SD ($n = 3$). $^{**}P < 0.01$. $^{***}P < 0.001$. ns, not significant. (B) Confocal microscopy images of Kim-1 (green) and Cy5-C-CA-DA or Cy5-SC-CA-DA (red) in HK-2 cells (scale bar = 20 μm). (C) Fluorescence microscopy images of Kim-1 (green) and Cy5-SC-CA-DA (red) on kidney sections from AKI-injured mice (scale bar = 50 μm).

(Supporting Information Fig. S9). The released S14 (retention time 4.3 min) maintained its original structure (Fig. 4F). At 48 h, the cumulative release rate of S14 was 23.6 ± 2.5% at pH 7.4, whereas it reached 62.0 ± 3.8% at pH 4.5, indicating that the pH-sensitive amide bonds of S14@SC-CA-DA micelles could be disrupted in an acidic environment, thereby realizing rapid release of S14 (Fig. 4G). However, there was no obvious drug release in S14@SC-DA at different pH values, and the result showed that free S14 carried out a rapid release at different pH within 12 h (Supporting Information Fig. S10). Overall, the prepared S14@SC-CA-DA nanodelivery system had a pH-responsive ability to quickly release drugs.

### *3.6. Cellular uptake, Kim-1-targeted ability and lysosome escape of micelles*

Before evaluating cellular internalization *in vitro*, the cytotoxicity of SC-CA-DA on HK-2 cells was performed using the cell counting Kit-8 (CCK-8) method (Supporting Information Fig. S11). The survival rate of SC-CA-DA-treated cells was above 95% when the concentration reached 250 μg/mL, indicating that SC-CA-DA is safe for biological application. DID@SC-CA-DA micelles were formed by encapsulating DID with the amphiphilic polymer SC-CA-DA, which is used to simulate the behavior of drugs in the body. The uptake capacities of DID/DID@SC-CA-DA in HK-2 cells with or without $H_2O_2$ for 2 and 6 h, were investigated by fluorescence microscope. As a result, there was no obvious difference in the fluorescence intensities between the DID groups with or without $H_2O_2$, for 2 or 6 h. However, $H_2O_2$-stimulated cells showed a much higher fluorescence intensity than normal cells when they were incubated with DID@SC-CA-DA for 6 h. Moreover, the fluorescence intensity of $H_2O_2$-stimulated cells was notably higher with DID@SC-CA-DA than with DID alone (Fig. 5A and Supporting Information Fig. S12). These results showed that HK-2 cells stimulated by $H_2O_2$ had a good uptake ability of DID@SC-CA-DA.

Kim-1 is mainly expressed in injured proximal tubules of the kidney. To investigate the association between the higher uptake of SC-CA-DA by $H_2O_2$-stimulated cells and Kim-1, an antibody blocking assay was performed (Fig. 5B), $H_2O_2$-stimulated cells pretreated with or without Kim-1 antibody blocker, were incubated with Cyanine-5 (Cy5)-SC-CA-DA for 6 h to assess kidney targeting ability. Cy5-SC-CA-DA is a Cy5-labeled amphiphilic polymer SC-CA-DA used to evaluate kidney targeting ability. Laser confocal results indicated that without Kim-1 antibody blocker, Cy5-SC-CA-DA treated cells had a stronger co-localization signal, indicating a specific interaction between Cy5-SC-CA-DA and Kim-1. In the presence of the Kim-1 antibody, the cellular internalization of Cy5-SC-CA-DA was slowed down, showing the red fluorescent signal was reduced in the cells. Therefore, less colocalization between Cy5-C-CA-DA and Kim-1 was observed. In contrast, the presence of the Kim-1 antibody had little effect on the cellular uptake of Cy5-C-CA-DA.

These findings confirmed that up-regulation of Kim-1 in injured kidney cells promoted cellular internalization of SC-CA-DA through a specific interaction between Kim-1 and SC-CA-DA. The kidney slices were collected at 4 h after tail vein injection of Cy5-SC-CA-DA in AKI mice, fluorescence microscopy showed clear colocalization of Kim-1 and Cy5-SC-CA-DA, further supporting the Kim-1-targeted ability of SC-CA-DA (Fig. 5C and Supporting Information Fig. S13).

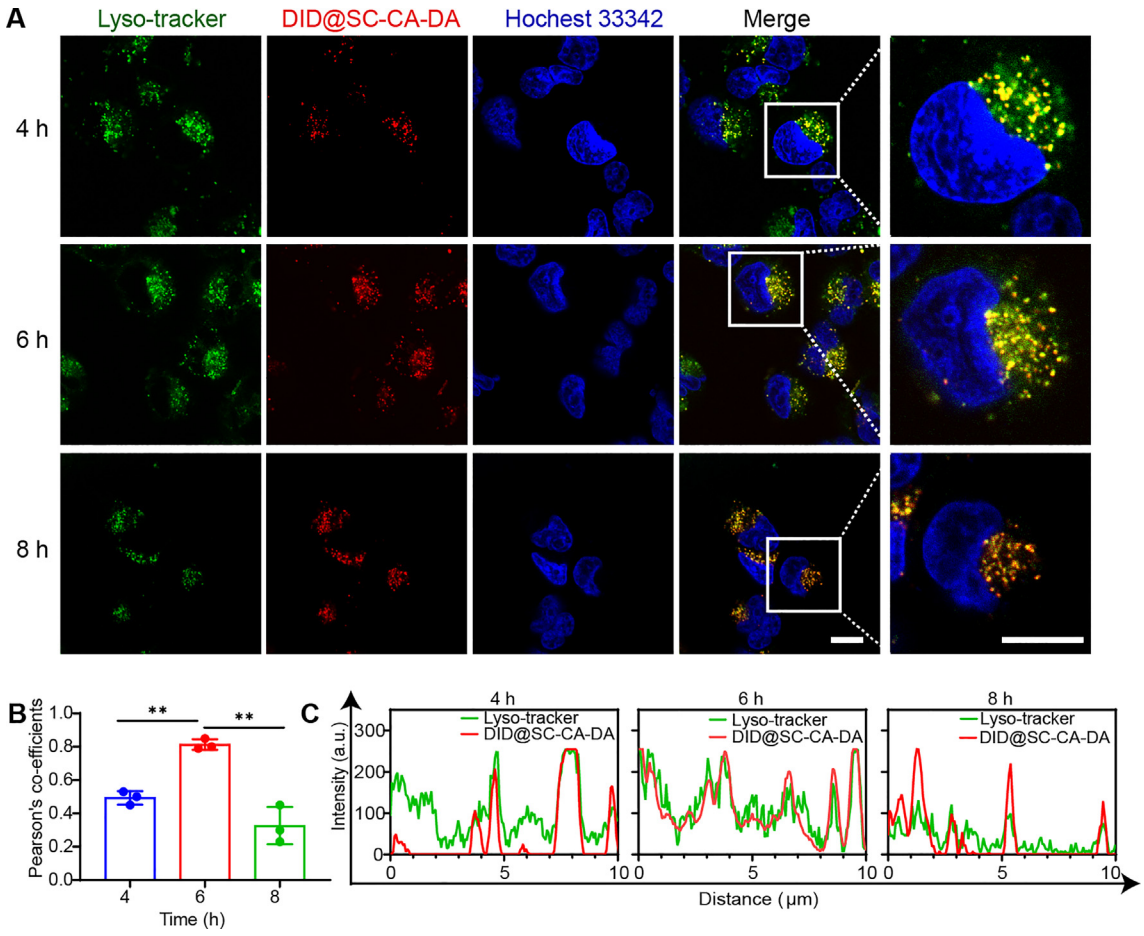


**Figure 6** Lysosome escape of S14@SC-CA-DA micelles. (A) Fluorescent images of HK-2 cells after incubating with DID or DID@SC-CA-DA, respectively, for 4, 6, and 8 h (scale bar = 10 μm). (B) Pearson correlation coefficients of DID and Lyso-Tracker green fluorescence intensity, The data are the means ± SD ($n$ = 3). $^{**}P < 0.01$. (C) The level of overlay of DID and Lyso-Tracker is green.

To monitor the intracellular dynamics of the micelles, we utilized LysoTracker Green to label the lysosome. CS, a positively charged polymer polysaccharide, possesses proton buffering ability to rupture lysosomes, facilitating the release of therapeutic drugs from the endosome to the cytosol through the "proton sponge effect"[26,45]. As shown in Fig. 6A, the micelles and lysosomes showed obvious co-localization at 6 h, which indicated DID@SC-CA-DA could reach lysosomes after cellular uptake. Furthermore, Image-Pro Plus software was employed for the semi-quantitative analysis of fluorescence intensity (Fig. 6B and C), with Pearson's coefficient of 0.81. As the time extended to 8 h, the co-localization of the signal from DID@SC-CA-DA with Lyso-tracker was significantly reduced, with Pearson's coefficient of 0.32. These results indicate that S14@SC-CA-DA can release S14 in the acidic lysosomal, and meanwhile, cause the lysosomal disruption by the proton sponge effect to enable transportation of the released S14 from endo-lysosomes to cytoplasm.

### *3.7. Anti-oxidative stress and anti-apoptosis by S14@SC-CA-DA in vitro*

When acute kidney injury occurs, ROS in renal tubular epithelial cells will increase abnormally, triggering mitochondrial damage[46]. The abilities of S14, S14@SC-DA and S14@SC-CA-DA to reduce mitochondrial ROS production in oxidatively stressed HK-2 cells were examined by a mitochondrial ROS probe (MitoSOX). The fluorescence intensity of MitoSOX was significantly higher in $H_2O_2$-stimulated HK-2 cells. However, the MitoSOX fluorescence intensity was significantly lower in cells treated with S14@SC-CA-DA compared to S14 and S14@SC-DA, indicating the obvious effects of S14@SC-CA-DA to scavenge ROS and alleviate oxidative stress (Fig. 7A and E).

Subsequently, changes in mitochondrial membrane potential (MMP) were detected by using JC-1 fluorescent dye. The decreased red/green fluorescence intensity ratio in the $H_2O_2$-incubated cells, indicating the decreased MMP caused by oxidative stress was significantly increased after the treatment with S14, S14@SC-DA and S14@SC-CA-DA (Fig. 7B and F). Notably, S14@SC-CA-DA had the strongest ability to stabilize MMP by alleviating mitochondrial oxidative stress, with a larger enhancement of red/green fluorescence intensity ratio than others.

Furthermore, the effect of S14@SC-CA-DA on cell apoptosis was examined by flow cytometry. As expected, $H_2O_2$-treated cells showed a significantly increased apoptosis rate, while the treatment of S14, S14@SC-DA and S14@SC-CA-DA markedly reduced cell apoptosis induced by $H_2O_2$ stimulation (Fig. 7D and K). Particularly, the S14@SC-CA-DA group exhibited the

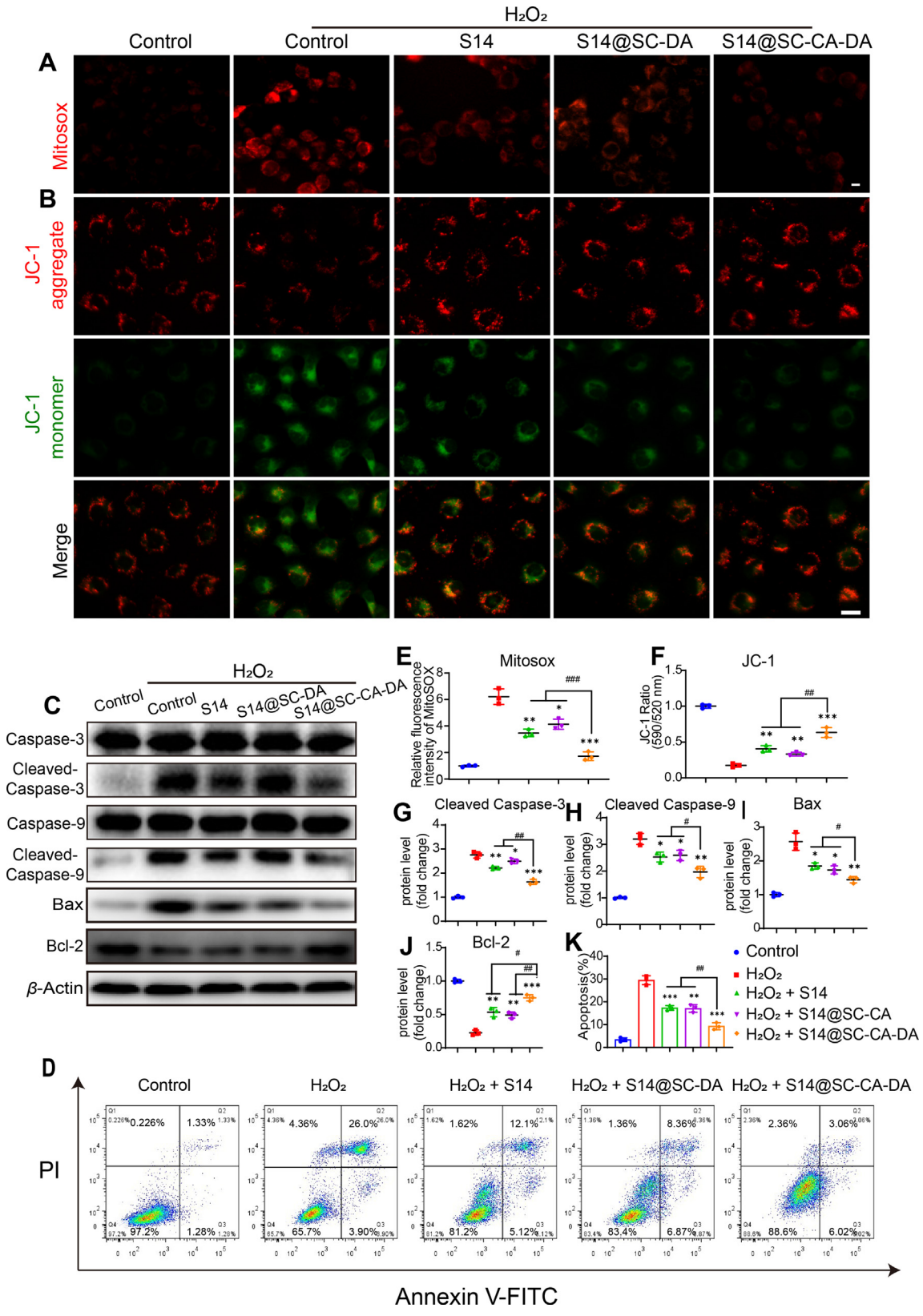


**Figure 7** S14@SC-CA-DA reduced oxidative stress and apoptosis *in vitro*. (A) Fluorescence images of mitochondrial ROS detected by MitoSOX (scale bar = 20 μm. (B) Fluorescence images of JC-1 staining in HK-2 cells (scale bar = 20 μm). (C) WB analysis of caspase-3, cleaved caspase-3, caspase-9, cleaved caspase-9, Bax, and Bcl-2 proteins in HK-2 cells. (D) Flow cytometric analysis of HK-2 cells using apoptosis detection kit. (E) The MitoSOX mean fluorescence intensity of (A). (F) The mean ratio of fluorescence intensity of JC-1 aggregates and

lowest apoptosis rate, indicating that S14@SC-CA-DA has a stronger ability to protect cells from apoptosis caused by oxidative stress. To further investigate the oxidative stress-induced mitochondrial-mediated apoptotic pathway, the levels of pro-apoptotic proteins, including cleaved caspase-3, cleaved caspase-9 and Bax, as well as the anti-apoptotic protein Bcl-2, were detected by Western blot. Semi-quantitative analysis was performed by image J (Fig. 7G−J). The expression levels of cleaved caspase-3, cleaved caspase-9 and Bax were increased, while the expression level of Bcl-2 was decreased in $H_2O_2$-stimulated cells. Notably, compared with the free S14 group, S14@SC-CA-DA significantly decreased the expression of cleaved caspase-3, cleaved caspase-9 and Bax, while increasing the expression of Bcl-2 expression. Additionally, S14@SC-CA-DA markedly reduced Kim-1 expression level, thus alleviating $H_2O_2$-induced cell injury. Consequently, S14@SC-CA-DA effectively ameliorated the mitochondrial apoptotic pathway and reduced renal tubular cell apoptosis.

### 3.8. *Treatment with S14@SC-CA-DA micelles in IR-induced AKI C57BL/6 mice*

The ability of S14@SC-CA-DA to alleviate AKI was investigated by an ischemia−reperfusion (IR)-induced AKI mice model. We chose unilateral left renal pedicle clamping-induced IR AKI mice as the animal model. After a 45-min ischemia period, the unilateral left clamps were released to restore blood flow. The treatment time points are shown in Fig. 8A.

To investigate the renal-targeting of micelles *in vivo*, IR-induced AKI mice were intravenously injected with DID and DID@SC-CA-DA. The fluorescence intensity of renal tissue was observed using an *ex vivo* imaging system at predetermined time points (2, 6, 12 and 24 h) after intravenous administration. Compared to the DID group, the renal fluorescence intensity of DID@SC-CA-DA significantly increased. Moreover, the fluorescence intensity of DID-labeled micelles was markedly higher in injured kidneys compared to normal kidneys. At 24 h, injured kidneys still had stronger fluorescence intensity, whereas the fluorescence signal in normal kidneys significantly decreased (Fig. 8B and C, Supporting Information Fig. S14). These results suggested that micelles could specifically target injured kidney and accumulation ability in injured kidneys. To further investigate the renal tubular targeting ability of SC-CA-DA, damaged kidneys from AKI mice were collected 4 h after tail vein injection of Cy5-SC-CA-DA, and the fluorescence distribution in kidney sections was observed. The fluorescence signal of Cy5 was rarely distributed in the glomerulus, mainly around the glomerulus, which is the location of the renal tubules (Supporting Information Fig. S15), indicating that Cy5-SC-CA-DA was mainly located in the renal tubules. Thus, its high accumulation in the renal tubules suggests that SC-CA-DA is a potential drug carrier for effective AKI therapy.

Elevated serum creatinine (Scr) and blood urea nitrogen (BUN) levels are valid clinical indicators of impaired renal function[47]. In the AKI model, Scr and BUN concentrations were significantly increased (4- and 3.5-fold to the control group, respectively). However, treatment with S14 and S14@SC-CA-DA effectively reduced the levels of Scr and BUN. Among these treatments, the S14@SC-CA-DA group showed the most significant effects, with a reduction of 64.69% and 45.20% in Scr and BUN levels, respectively, indicating the significant renal function improvement achieved by S14@SC-CA-DA in AKI mice (Fig. 8D and E). Furthermore, the therapeutic effects of S14@SC-CA-DA were assessed through kidney section tissue analysis using H&E staining. As shown in Fig. 8F, the model group presented typical histological characteristics of AKI, including necrosis and detachment of renal tubular epithelial cells, formation of cellular debris or hyaline casts in the tubular lumen (red arrows), and cellular vacuolization (green arrows). While cell detachment and local necrosis were still observed in the kidney tissue of S14-treated mice. Treatment with S14@SC-CA-DA exhibited a more significant effect in reducing the damage.

### 3.9. *In vivo therapeutic mechanisms of S14@SC-CA-DA*

The reabsorption capacity of renal tubules, facilitated by protective mitochondria, is crucial for restoring renal function[48]. In healthy renal tissue, the tubular region exhibits a high density of mitochondria to meet the energy demands associated with tubular processes[49]. Transmission electron microscopy (TEM) images of renal tissues revealed mitochondrial damage in renal tubular cells caused by AKI, manifested by mitochondrial swelling, loss of cristae, and even membrane rupture, resulting in the efflux of matrix material into the cytoplasm (Fig. 9A). Treatment with S14, S14@SC-DA and S14@SC-CA-DA significantly reduced mitochondrial damage in renal tubular cells of AKI mice. S14@SC-CA-DA exhibited the least number of damaged mitochondria, with most mitochondria maintaining a relatively intact cristae structure. These results indicate that S14@SC-CA-DA micelles could better protect mitochondria.

To further evaluate the antioxidant stress effect of S14@SC-CA-DA in AKI kidneys, malondialdehyde (MDA), the decomposition product of peroxidized polyunsaturated fatty acids, was measured as an indicator of ROS damage[50-52]. Compared with the sham group, the MDA level in the plasma of AKI mice was significantly increased (Fig. 9I). Treatment with S14, S14@SC-DA and S14@SC-CA-DA reduced the MDA level in AKI model mice, with the S14@SC-CA-DA group exhibiting the lowest level of MDA. It was further indicated that S14@SC-CA-DA had the best antioxidant ability *in vivo*. When AKI occurs, macrophages will migrate to the injured kidney and release pro-inflammatory factors to trigger an inflammatory response. To evaluate the anti-inflammatory effect of S14@SC-CA-DA in AKI kidney, the levels of proinflammatory cytokines interleukin-6 (IL-6) and tumor necrosis factor-$\alpha$ (TNF-$\alpha$) were measured in plasma (Fig. 9J and K). The AKI group showed significantly increased levels of IL-6 and TNF-$\alpha$. Treatment with S14, S14@SC-DA and S14@SC-CA-DA resulted in decreased expression levels of IL-6 and TNF-$\alpha$. Among the treatment groups, S14@SC-CA-DA exhibited the lowest cytokine levels, indicating its potent anti-inflammatory ability.

Apoptotic cells in AKI-injured kidneys were detected using the TUNEL assay. Compared to the sham group, the number of apoptotic cells in the kidneys of AKI mice was significantly

JC-1 monomers in (B). (G−J) Quantification of the protein immunoblots of cleaved caspase-3, cleaved caspase-9, Bax, and Bcl-2. (K) Apoptosis rate in various groups. Data are the means ± SD ($n = 3$). $^{*}P < 0.05$, $^{**}P < 0.01$ and $^{***}P < 0.001$ as compared with $H_2O_2$ group. $^{\#}P < 0.05$, $^{\#\#}P < 0.01$ and $^{\#\#\#}P < 0.001$ between groups as indicated.

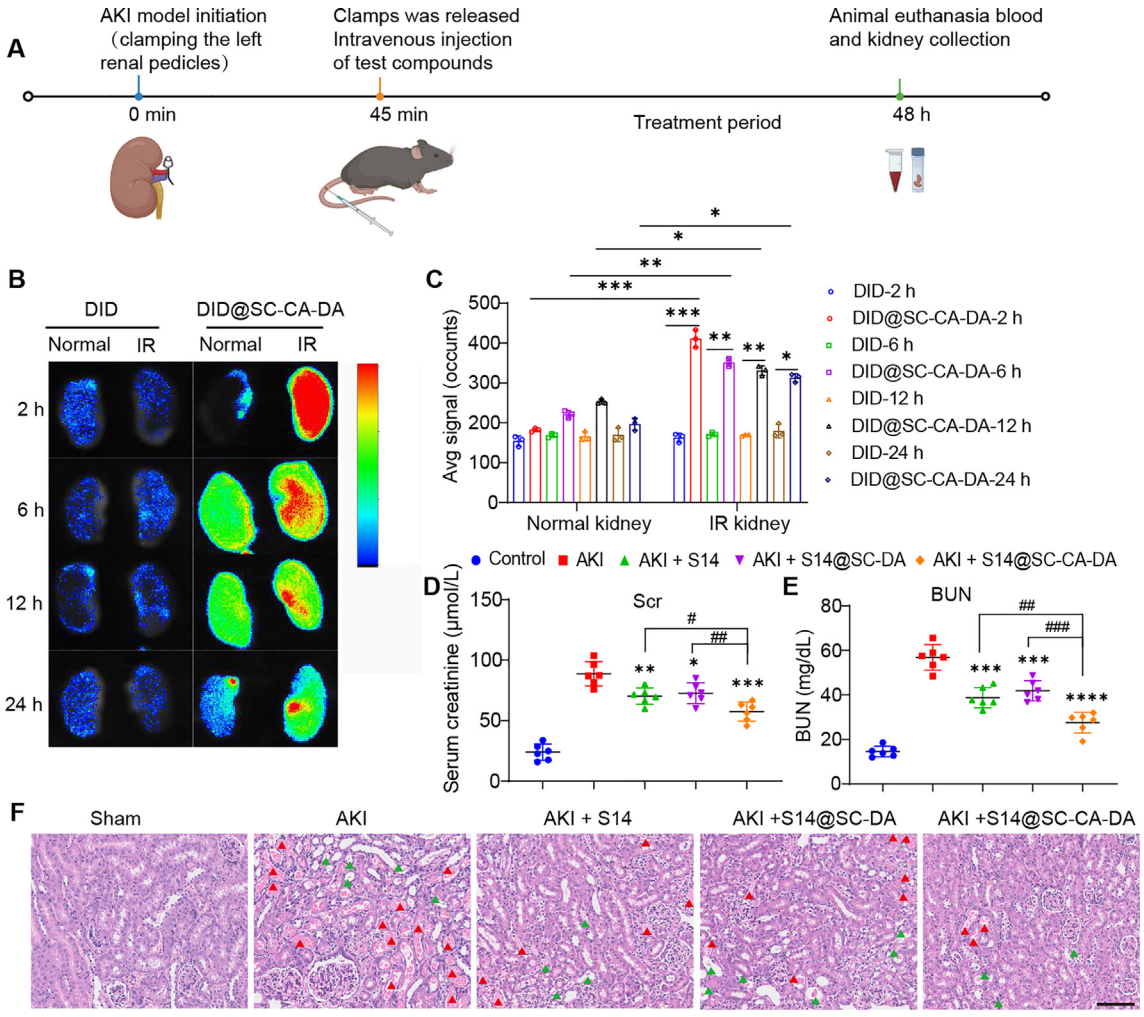


**Figure 8** Efficacy of S14@SC-CA-DA in the alleviation of renal function *in vivo*. (A) Schematic diagram of the establishment and treatment of an AKI model in C57BL/6 mice. (B) The kidney fluorescence imaging of DID and DID@SC-CA-DA at 2, 6, 12, and 24 h. (C) Mean fluorescence intensity of kidney. Data are mean ± SD ($n = 3$). (D, E) Serum analysis of creatinine (D) and BUN (E) levels. Data are mean ± SD ($n = 6$). (F) H&E staining of kidney tissues (scale bar = 100 μm). Renal tubular vacuolization (green arrows). Red arrowheads donate renal tubular epithelial cell necrosis and sloughing, forming cellular debris or casts. $^{*}P < 0.05$, $^{**}P < 0.01$, $^{***}P < 0.001$ and $^{****}P < 0.0001$ as compared with saline. $^{\#}P < 0.05$, $^{\#\#}P < 0.01$ and $^{\#\#\#}P < 0.001$ between groups as indicated.

increased. Treatment with S14, S14@SC-DA, and S14@SC-CA-DA reduced AKI-induced apoptosis, with the S14@SC-CA-DA group exhibiting the fewest apoptotic cells (Fig. 9B and D). Furthermore, the expression levels of pro-apoptotic proteins, including cleaved caspase-3, cleaved caspase-9, and Bax, as well as the anti-apoptotic protein Bcl-2 in kidney tissue, were detected by Western blot (Fig. 9C), The quantitative analysis was performed by image J (Fig. 9E−H), which showed that S14@SC-CA-DA effectively reduced apoptosis in kidney tissue of IR-AKI. These results collectively indicate the superior anti-apoptotic effect of S14@SC-CA-DA.

### *3.10. Pharmacokinetics and safety evaluation*

The majority of drugs undergo metabolic reactions catalyzed by metabolic enzymes upon entering the body. In this study, we conducted the phase I cytochrome P450 (CYP) and phase II UDP-glucuronosyltransferase (UGT) metabolism of S14 in human liver microsomes. The elimination rate of S14 is 7.38 times higher in UGT metabolism than that in CYP metabolism (Fig. 10A), indicating predominant UGT-mediated metabolism of S14 (Fig. 10B). Mono-glucuronides were identified as metabolites using LC−MS/MS (Supporting Information Fig. S16). To assess the pharmacokinetic behavior of S14 and S14@SC-CA-DA (S14 equivalent: 2 mg/kg), we evaluated their plasma concentrations in C57BL/6 mice. Plasma samples were collected at specified time points following intravenous injection, and the plasma drug concentration−time curves are shown in Fig. 10C. Pharmacokinetic parameters (Table S5) revealed that the area under the curve ($AUC_{0-t}$) of S14@SC-CA-DA (53.33 ± 3.63 mg/L·min) was higher than that of S14 (21.79 ± 1.36 mg/L·min), while the half-life time ($t_{1/2}$) of free S14 (26.57 ± 5.97 min) was prolonged by S14@SC-CA-DA (47.12 ± 11.48 min). These results indicate that S14@SC-CA-DA exhibited a longer circulation lifetime than S14. Additionally, the presence of S14-Glu in plasma indicated that S14@SC-CA-DA retarded the UGT metabolism of S14

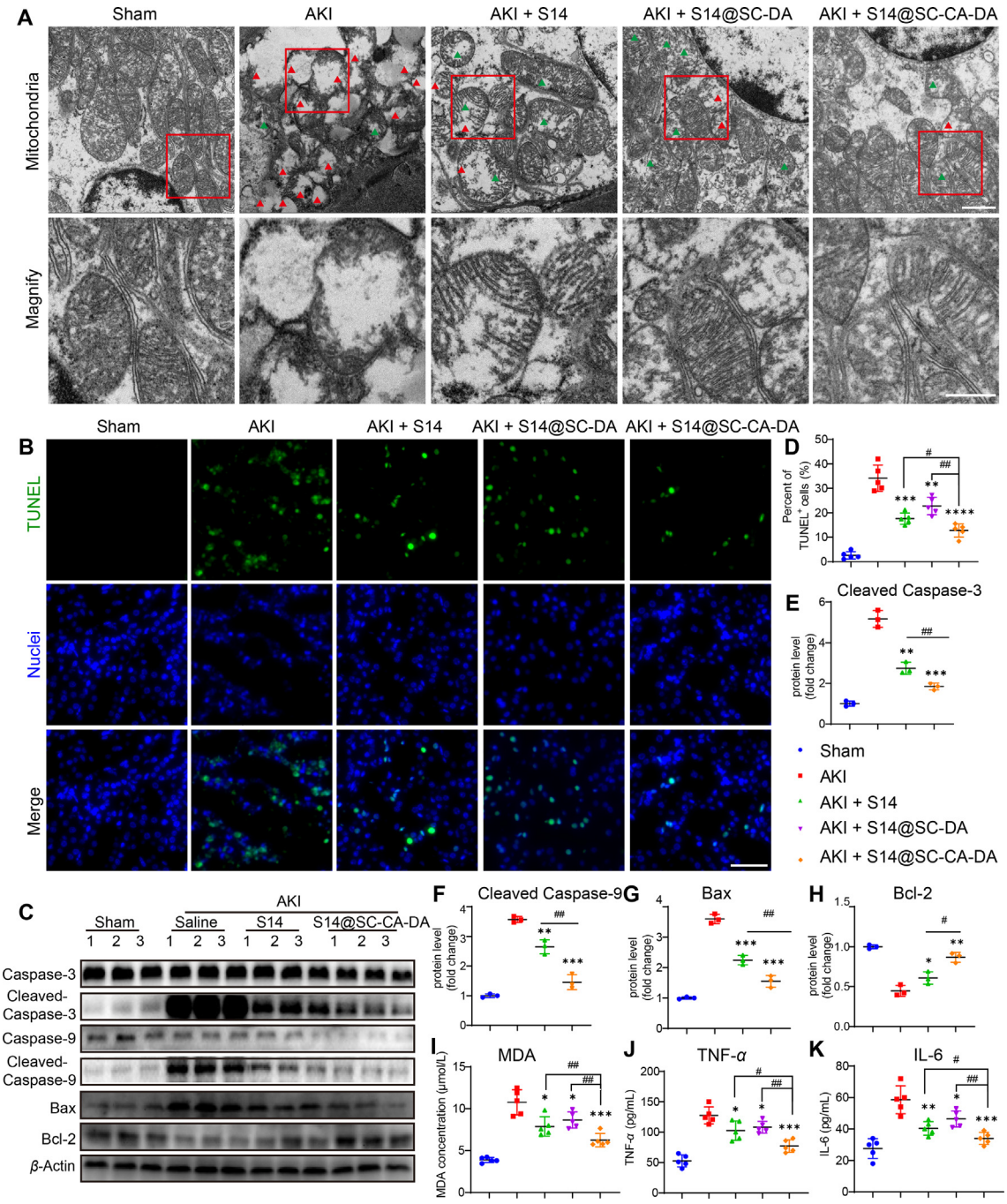


**Figure 9** S14@SC-CA-DA protects mitochondria from damage and reduces oxidative stress, inflammation, and apoptosis in AKI mice. (A) Bio-TEM image of mitochondria of tubular cells (scale bar = 1 μm), Zoom out image (scale bar = 500 nm) is shown. Swollen mitochondrion with disturbed cristae structure (green arrowheads). The mitochondrial membrane ruptures and matrix material is released into the cytoplasm (red arrowheads). (B) TUNEL staining (scale bar = 50 μm). (C) WB analysis of caspase-3, cleaved caspase-3, Caspase-9, cleaved caspase-9, Bax, and Bcl-2 proteins in kidney tissue. (D) Quantification of TUNEL-positive cells in (B). (E−H) Quantification of the protein immunoblots of cleaved caspase-3, cleaved caspase-9, Bax, and Bcl-2. Data are mean ± SD ($n = 3$). (I−K) MDA, TNF-$\alpha$, and IL-6 level changes in AKI mice after different treatments. Data are mean ± SD ($n = 5$). $^{*}P < 0.05$, $^{**}P < 0.01$, $^{***}P < 0.001$ and $^{****}P < 0.0001$ as compared with saline. $^{\#}P < 0.05$ and $^{\#\#}P < 0.01$ between groups as indicated.

(Fig. 10D). These findings demonstrate that S14@SC-CA-DA could improve the pharmacokinetics behavior of S14.

Furthermore, we examined the kidney-targeting capability of S14@SC-CA-DA in AKI. LC−MS/MS analysis was performed to measure the concentration of S14 in major organs (heart, liver, spleen, lung and kidney) of AKI mice. At 30 and 150 min after the S14 dose of 2 mg/kg, the concentration of S14 in the AKI kidney was significantly higher in the S14@SC-CA-DA group compared to the S14 group (Fig. 10E) (30 min, S14@SC-CA-DA, 41.34 ± 13.24 ng/mL, S14, 15.30 ± 7.31 ng/mL; 150 min,

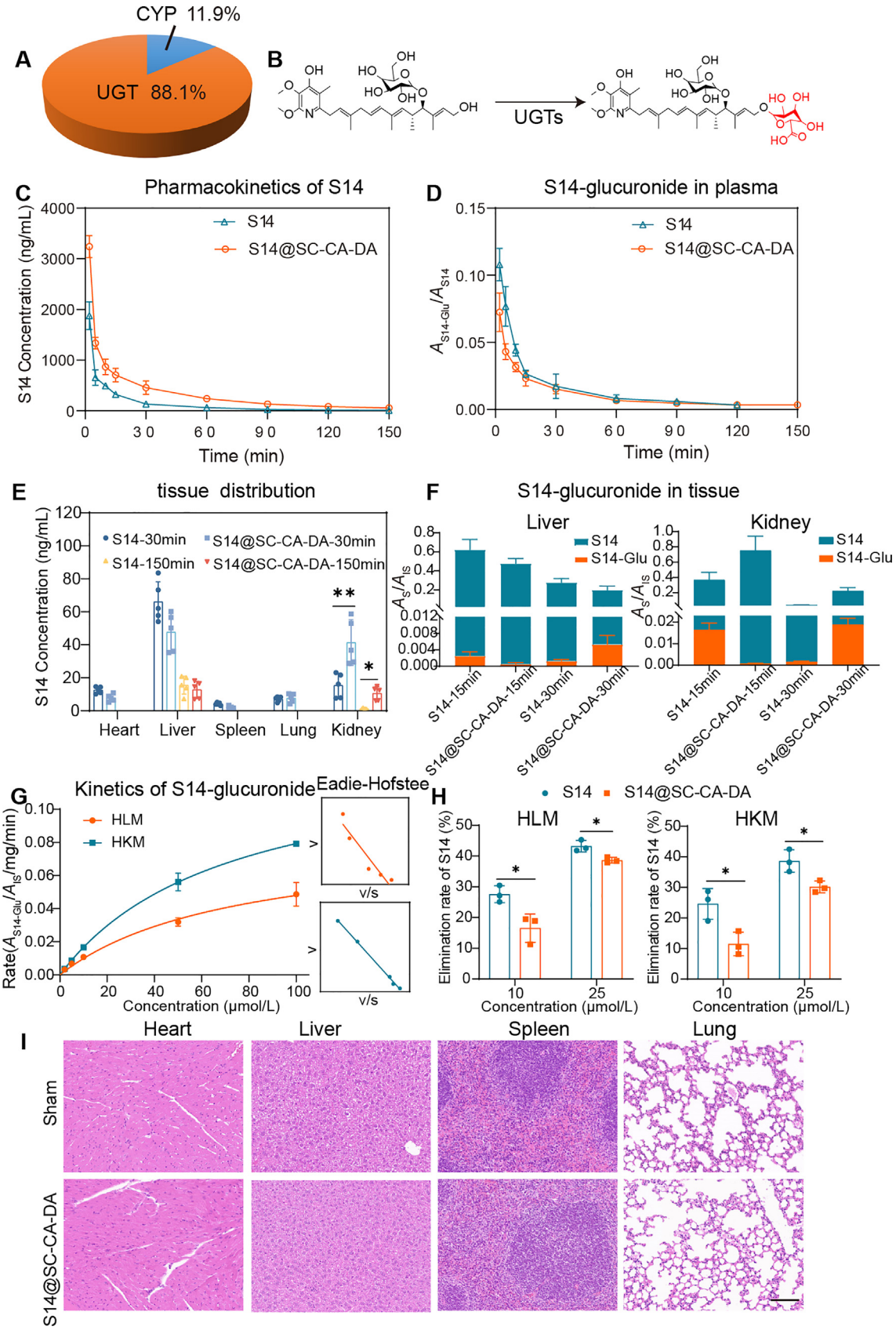


**Figure 10** Pharmacokinetics, tissue distribution, metabolism, and safety evaluation of S14@SC-CA-DA. (A) CYP and UGT contribution of S14 in human liver microsome. (B) The reaction formula generates S14-glucuronide. (C) Mean plasma concentration *vs.* time profiles of S14 and S14@SC-CA-DA. (D) S14-glucuronide of S14 and S14@SC-CA-DA in plasma. (E) tissue distribution profile. (F) S14-glucuronide of S14 and

S14@SC-CA-DA, 10.55 ± 4.08 ng/mL, S14, 1.28 ± 0.44 ng/mL), which was consistent with the fluorescence results in Fig. 6B. Hence, S14@SC-CA-DA demonstrates its superior ability as a kidney-targeted drug for AKI. The presence of S14-Glu was detected in the liver and kidney tissues, with higher levels of S14-Glu in S14 compared to S14@SC-CA-DA at 15 min, while S14-Glu of S14 was metabolized quickly at 30 min (Fig. 10F). These results indicate that S14@SC-CA-DA retards the UGT metabolism of S14 and reduces the clearance rate of S14 in mice. To investigate the biotransformation of S14 in liver and kidney microsomes, we performed concentration-dependent experiments and analyzed the kinetics of S14 glucuronidation using Eadie-Hofstee plots (Fig. 10G). The enzymatic kinetic parameters are shown in Table S6. The results demonstrate that S14 is metabolized in both liver and kidney microsomes.

To further verify that S14@SC-CA-DA retards the UGT metabolism of S14, incubation experiments were performed using human liver and kidney microsomes. It demonstrated that the elimination rate of S14 in S14@SC-CA-DA was lower than S14 group (1.84-fold in HLM, and 2.26-fold in HK (Fig. 10H). Finally, we investigated the potential toxicity of the micelles by performing H&E staining on major organs. As shown in Fig. 10I, there were no significant morphological abnormalities were observed in any of the tissues. The nephrotoxicity of S14 and S14@SC-CA-DA was also evaluated after 3 and 7 days (Supporting Information Fig. S17), and the results from HE staining demonstrated the absence of nephrotoxicity from both S14 and S14@SC-CA-DA.

## 4. Discussion

In the study, we proposed a systematic marine drug developmental strategy, encompassing the identification of new therapeutic targets and the design of novel drugs based on ADME characteristics. This innovative system boasts several key features: (i) exploration of new targets for marine drugs, (ii) specific targeting ability of Kim-1, (iii) improvement in ADME characteristics (kidney distribution, $AUC_{0-t}$, $t_{1/2}$, biotransformation, and UGT-mediated metabolism). These features collectively help us to improve the renal biodistribution and pharmacokinetics of drugs for better efficacy and effectiveness.

The marine-derived piericidin glycoside S14 has demonstrated significant therapeutic potential against AKI[16]. In this study, we revealed that S14 possess a protective role on AKI *via* activating PRDX1. PRDX1, known as an effective antioxidant enzyme, which against inducible oxidative stress within ischemia−reperfusion[36]. *Prdx1*-OE mice were applied to reveal the protective effect of S14 depending on PRDX1 activation. Compared to Control mice, we found that UIRI-induced kidney injury was significantly reduced in *Prdx1*-OE mice. Therefore, PRDX1 activation may be considered a new therapeutic target in AKI. Further investigation using SPR and CETSA-WB analysis explored the binding of S14 to PRDX1. The results supported PRDX1 as the direct binding target of S14, with S14 mainly binding to Cys83 of PRDX1 (Fig. 3D), it is speculated that S14 prevents decamer formation and increases peroxidase activity (Supporting Information Fig. S18). Additionally, S14 promotes PRDX1 nuclear translocation and facilitates the binding of PRDX1 to nuclear transcriptional factors Nrf2 (Fig. 2Q and R). Previous studies have shown that promoting the entry of Nrf2 into the nucleus can activate the Nrf2/HO-1/NQO1 pathway to inhibit ROS production[53]. Moreover, our study revealed that Nrf2 expression was suppressed even after adding S14 when PRDX1 was knocked down. These findings collectively suggest that S14 could be considered as a lead compound targeting PRDX1 and regulating PRDX1/Nrf2 to reduce ROS levels. And immunoprecipitation experiments to demonstrate the association between PRDX1 and LKB1. The results showed no interaction between PRDX1 and LKB-1 (Supporting Information Fig. S19). Bioactive marine natural products (MNPs) have shown promise as potential candidates for drug development. However, challenges such as hydrophobicity, toxicity, nontargeting behavior, and limited bioavailability have impeded the development of marine drug candidates[54]. For instance, marine-derived piericidin glycoside S14 has been revealed with obvious therapeutic potential against AKI in our previous study. Glycosides, compared to the hepatotoxic piericidin aglycone, exhibit lower toxicity[16]. However, S14 suffers from a short half-life, poor bioavailability (2.6%), low targeting specificity, and rapid biotransformation, prompting the need for a delivery system that enhances the druggability of piericidin glycosides (Figs. S1 and S16, Table S1).

Thus, we designed a pH-sensitive Kim-1-targeted SC-CA-DA polymer to improve the druggability of the marine drug candidate S14. *In vitro* drug release experiments were conducted at different pH for simulate the corresponding physiological environment (Fig. 4B). The free S14 solution showed a rapid release of S14 at pH 7.4, and almost 80% of S14 was released within 12 h (Supporting Information Fig. S10). In contrast, S14-loaded SC-CA-DA and SC-DA micelles exhibited a slower release of S14 at pH 7.4, with only 15% of the total S14 released at 12 h. At pH 4.5, no acceleration in S14 release was observed for SC-DA micelles, while S14 release from SC-CA-DA micelles was significantly accelerated, with 50% S14 being released after 12 h. This is likely due to the disassembly of micelles induced by pH values, also noticed that different pH values did not affect the release kinetics of S14@SC-DA. These results suggested that S14@SC-CA-DA are stable in the blood circulation environment, but are triggered to release S14 rapidly in response to the acid environment after intracellular uptake. The presence of a double bond in the citrate amide facilitates the cleavage of the amide bond, allowing for efficient drug release. Intracellular studies have confirmed that S14@SC-CA-DA can release S14 in acidic lysosomes, causing lysosomal disruption through the proton sponge effect, enabling the transportation of released S14 from endo-lysosomes to the cytoplasm (Fig. 6). Then the S14 binding to the PRDX1, instead of S14@SC-CA-DA binding to PRDX1 (Supporting Information Figs. S20 and S21). Furthermore, we demonstrated that S14@SC-CA-DA exhibits exceptional kidney targeting, attributed to its preferential internalization by damaged renal tubular cells through Kim-1-mediated endocytosis. Kim-1 has attracted much attention in the early diagnosis and pathological mechanism of kidney disease[55,56]. *In vivo* studies revealed that the nanodelivery system significantly enhances the therapeutic

S14@SC-CA-DA in tissue. (G) Kinetics of S14-glucuronide in human liver microsome (HLM) and human kidney microsome (HKM) at different concentrations. Data are mean ± SD ($n = 3$). (H) Elimination rate of S14 in human liver microsome (HLM) and human kidney microsome (HKM). (I) H&E staining of major organs after treatment (scale bar = 100 μm). Data are mean ± SD ($n = 5$). *$P < 0.05$ and **$P < 0.01$.

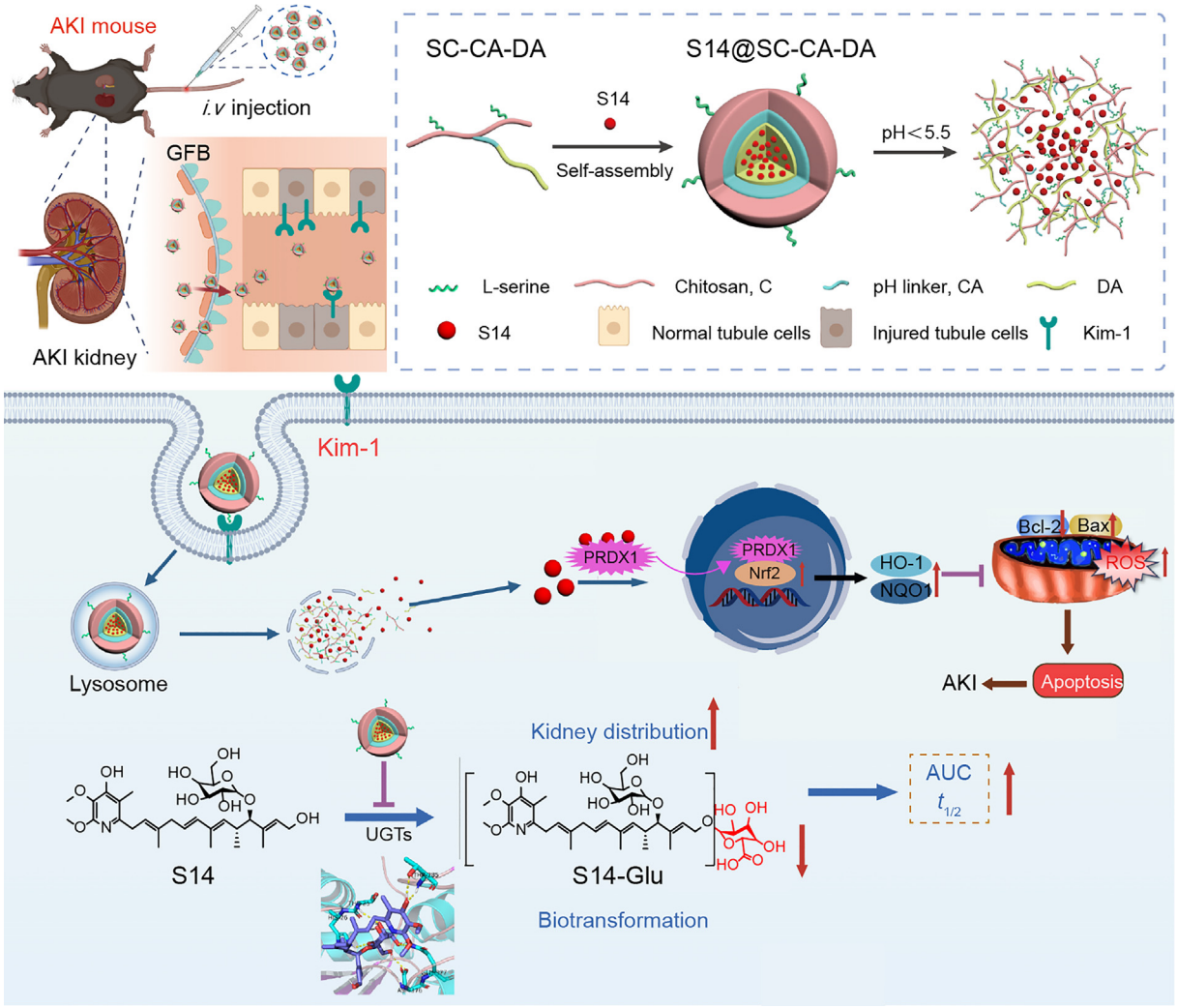


**Figure 11** Schematic illustration of S14@SC-CA-DA for alleviating AKI. After intravenous administration, S14@SC-CA-DA travels through the bloodstream to the injured kidney. Overexpression of Kim-1 in injured renal tubular cells enhances the internalization of S14@SC-CA-DA. In the acidic microenvironment of the AKI kidney, S14@SC-CA-DA pH-dependent releases S14, S14 targets PRDX1 and regulates PRDX1/Nrf2 to reduce ROS levels, promotes the restoration of mitochondrial homeostasis and improves pharmacokinetics behavior of S14, thereby ameliorates AKI.

effect of S14, promoting kidney function recovery (with a 64.69% reduction in Scr and a 45.20% reduction in BUN compared to sham, Fig. 8D and E). The nanodrugs effectively alleviate oxidative stress, protect mitochondria, mitigate inflammation, and reduce apoptosis. The high therapeutic efficiency of S14 nanodrugs stems from their precise accumulation and sensitive release in the injured kidney (Fig. 8B).

To further evaluate the druggability of S14-nanodrug, we assessed their pharmacokinetic behavior. The results showed that S14 nanodrugs prolong the plasma half-life and AUC of S14. Tissue distribution indicated that the concentration of S14 in nanodrugs was 3.1-fold higher than that of bare S14 (Fig. 10E). We also observed that UGT-mediated metabolism plays a predominant role in the biotransformation of S14 in the liver and kidney. To confirm that S14-nanodrug alleviate UGT-mediated metabolism in human liver and kidney microsomes, we demonstrated that the elimination rate of S14 in nanodrugs was lower than that in the S14 group (1.84-fold in human liver microsomes and 2.26-fold in human kidney microsomes, Fig. 10H). These findings suggest that nanodrugs retard the UGT-mediated metabolism of S14, leading to decreased elimination rates and increased levels of the parent drug. Moreover, the biosafety of the nanodrug was assessed, and no obvious abnormalities were found in the major organs, demonstrating no nephrotoxicity.

## 5. Conclusions

In summary, our study presents a systematic approach to the development of marine drugs, integrating the discovery of novel therapeutic targets and the design of optimized drug formulations based on pharmacokinetic properties. We have demonstrated that S14 possesses a protective role in AKI by activating PRDX1, mainly binding to Cys83 of PRDX1 and increasing the peroxidase activity. S14 increases the PRDX1 nuclear translocation and activates the Nrf2/HO-1/NQO1 pathway, resulting in the inhibition of ROS production. Based on the pharmacokinetics properties, we

reveal that the pH-sensitive Kim-1-targeted nanodelivery system is a versatile strategy for precise AKI therapy (Fig. 11). The modified marine polysaccharides based nanocarrier enhances the efficacy and the druggability of marine-derived drug candidates with a hydrophobic chain, The nanodrugs improve ADME properties by increasing plasma half-life, AUC and kidney distribution, and retard the UGT-mediated metabolism of S14. Consequently, our research may provide a constructive strategy for the clinical development of a new and effective treatment method for AKI.

## Acknowledgments

This work was supported by the Guangdong Local Innovation Team Program (2019BT02Y262, China), National Natural Science Foundation of China (U20A20101, 82274002, 22175083), Key-Area Research and Development Program of Guangdong Province (2023B1111050008, China), National Key Research and Development Program of China (2022YFA1206900, 2023YFA0914200), Science and Technology Innovation Project of Guangdong Medical Products Administration (S2021ZDZ042, 2023ZDZ06, 2024ZDZ08, China).

## Author contributions

Ping Yu and Tanwei Gu contributed equally to this work. Conceived the study: Yingfeng Tu, Lan Tang, Xuefeng Zhou; Anti-AKI mechanism: Ping Yu, Tanwei Gu; Preparation of micelles: Ping Yu, Yueyang Rao; Animal experiment: Ping Yu, Huanguo Jiang, Jianmin Guo; PK/ADME: Ping Yu, Weimin Liang, Xi Zhang, Jindi Lu; Preparation of S14: Jianglian She; Data analysis: Ping Yu, Yingfeng Tu, Lan Tang; Visualization: Ping Yu; Supervision: Wei Yang, Yonghong Liu, Yingfeng Tu, Lan Tang, Xuefeng Zhou; Writing—original draft: Ping Yu; Writing—editing: Yingfeng Tu, Lan Tang, Xuefeng Zhou.

## Conflicts of interest

The authors declare no conflicts of interest.

## Appendix A. Supporting information

Supporting information to this article can be found online at https://doi.org/10.1016/j.apsb.2024.03.005.

## References

1. Bellomo R, Kellum JA, Ronco C. Acute kidney injury. *Lancet* 2012;**380**:756−66.
2. Poston JT, Koyner JL. Sepsis associated acute kidney injury. *BMJ* 2019;**364**:k4891−908.
3. Gerhardt LMS, Liu J, Koppitch K, Cippà PE, McMahon AP. Single-nuclear transcriptomics reveals diversity of proximal tubule cell states in a dynamic response to acute kidney injury. *Proc Natl Acad Sci U S A* 2021;**118**:e2026684118.
4. Linkermann A, Chen G, Dong G, Kunzendorf U, Krautwald S, Dong Z. Regulated cell death in AKI. *J Am Soc Nephrol* 2014;**25**:2689−701.
5. Agarwal A, Dong Z, Harris R, Murray P, Parikh SM, Rosner MH, et al. Cellular and molecular mechanisms of AKI. *J Am Soc Nephrol* 2016;**27**:1288−99.
6. Gonsalez SR, Cortes AL, da Silva RC, Lowe J, Prieto MC, Lara LD. Acute kidney injury overview: from basic findings to new prevention and therapy strategies. *Pharmacol Therapeut* 2019;**200**:1−12.
7. Gao L, Zhong X, Jin J, Li J, Meng XM. Potential targeted therapy and diagnosis based on novel insight into growth factors, receptors, and downstream effectors in acute kidney injury and acute kidney injury-chronic kidney disease progression. *Signal Transduct Tar* 2020;**5**:9.
8. Pickkers P, Mehta RL, Murray PT, Joannidis M, Molitoris BA, Kellum JA, et al. Effect of human recombinant alkaline phosphatase on 7-day creatinine clearance in patients with sepsis-associated acute kidney injury a randomized clinical trial. *JAMA* 2018;**320**:1998−2009.
9. Palevsky PM, Liu KD, Brophy PD, Chawla LS, Parikh CR, Thakar CV, et al. KDOQI US commentary on the 2012 KDIGO clinical practice guideline for acute kidney injury. *Am J Kidney Dis* 2013;**61**:649−72.
10. Lameire N, Kellum JA, Grp KAGW. Contrast-induced acute kidney injury and renal support for acute kidney injury: a KDIGO summary (Part 2). *Crit Care* 2013;**17**:1−13.
11. Liu Q, Yao F, Chooi YH, Kang Q, Xu W, Li Y, et al. Elucidation of Piericidin A1 biosynthetic locus revealed a thioesterase-dependent mechanism of alpha-pyridone ring formation. *Chem Biol* 2012;**19**:243−53.
12. Trost BM, Gholami H. Propene as an atom-economical linchpin for concise total synthesis of polyenes: piericidin A. *J Am Chem Soc* 2018;**140**:11623−6.
13. Zhou X, Liang Z, Li K, Fang W, Tian Y, Luo X, et al. Exploring the natural piericidins as anti-renal cell carcinoma agents targeting peroxiredoxin 1. *J Med Chem* 2019;**62**:7058−69.
14. Li K, Liang Z, Chen W, Luo X, Fang W, Liao S, et al. Iakyricidins A−D, antiproliferative piericidin analogues bearing a carbonyl group or cyclic skeleton from *Streptomyces iakyrus* SCSIO NS104. *J Org Chem* 2019;**84**:12626−31.
15. Li K, Su Z, Gao Y, Lin X, Pang X, Yang B, et al. Cytotoxic minor piericidin derivatives from the actinomycete strain *Streptomyces psammoticus* SCSIO NS126. *Mar Drugs* 2021;**19**:428−42.
16. Liu C, Wang X, Wang X, Zhang Y, Min W, Yu P, et al. A new LKB1 activator, piericidin analogue S14, retards renal fibrosis through promoting autophagy and mitochondrial homeostasis in renal tubular epithelial cells. *Theranostics* 2022;**12**:7158−79.
17. Malek M, Nematbakhsh M. Renal ischemia/reperfusion injury; from pathophysiology to treatment. *J Renal Inj Prev* 2015;**4**:20−7.
18. Han SJ, Lee HT. Mechanisms and therapeutic targets of ischemic acute kidney injury. *Kidney Res Clin Pract* 2019;**38**:427−40.
19. Kuusniemi AM, Lapatto R, Holmberg C, Karikoski R, Rapola J, Jalanko H. Kidneys with heavy proteinuria show fibrosis, inflammation, and oxidative stress, but no tubular phenotypic change. *Kidney Int* 2005;**68**:121−32.
20. Barrera G. Oxidative stress and lipid peroxidation products in cancer progression and therapy. *ISRN Oncol* 2012;**2012**:137289−310.
21. Ichimura T, Bonventre JV, Bailly V, Wei H, Hession CA, Cate RL, et al. Kidney injury molecule-1 (KIM-1), a putative epithelial cell adhesion molecule containing a novel immunoglobulin domain, is up-regulated in renal cells after injury. *J Biol Chem* 1998;**273**:4135−42.
22. Uchida Y, Ke B, Freitas MC, Ji H, Zhao D, Benjamin ER, et al. The emerging role of T cell immunoglobulin mucin-1 in the mechanism of liver ischemia and reperfusion injury in the mouse. *Hepatology* 2010;**51**:1363−72.
23. Matsuura S, Katsumi H, Suzuki H, Hirai N, Hayashi H, Koshino K, et al. L-Serine-modified polyamidoamine dendrimer as a highly potent renal targeting drug carrier. *Proc Natl Acad Sci U S A* 2018;**115**:10511−6.
24. Hsu YT, Kao CY, Ho MH, Lee SP. To control floating drug delivery system in a simulated gastric environment by adjusting the Shell layer formulation. *Biomater Res* 2021;**25**:31.
25. Anusha JR, Fleming AT, Arasu MV, Kim BC, Al-Dhabi NA, Yu KH, et al. Mechanochemical synthesis of chitosan submicron particles from the gladius of todarodes pacificus. *J Adv Res* 2016;**7**:863−71.
26. Tang WM, Panja S, Jogdeo CM, Tang S, Ding L, Yu A, et al. Modified chitosan for effective renal delivery of siRNA to treat acute kidney injury. *Biomaterials* 2022;**285**:121562.

27. Yang CX, Nilsson L, Cheema MU, Wang Y, Frokiaer J, Gao S, et al. Chitosan/siRNA nanoparticles targeting cyclooxygenase type 2 attenuate unilateral ureteral obstruction-induced kidney injury in mice. *Theranostics* 2015;**5**:110−23.
28. Liu D, Shu GF, Jin FY, Qi J, Xu XL, Du Y, et al. ROS-responsive chitosan-SS31 prodrug for AKI therapy *via* rapid distribution in the kidney and long-term retention in the renal tubule. *Sci Adv* 2020;**6**: eabb7422.
29. Bugarski M, Ghazi S, Polesel M, Martins JR, Hall AM. Changes in NAD and lipid metabolism drive acidosis-induced acute kidney injury. *J Am Soc Nephrol* 2021;**32**:342−56.
30. Li J, Zhao MY, Xiang XY, He QN, Gui R. A novel biomimetic nanomedicine system with anti-inflammatory and anti-osteoporosis effects improves the therapy efficacy of steroid-resistant nephrotic syndrome. *J Nanobiotechnol* 2021;**19**:417.
31. Dong L, Krewson EA, Yang LV. Acidosis activates endoplasmic reticulum stress pathways through GPR4 in human vascular endothelial cells. *Int J Mol Sci* 2017;**18**:278.
32. Mindell JA. Lysosomal acidification mechanisms. *Annu Rev Physiol* 2012;**74**:69−86.
33. Bu Y, Zhang L, Sun G, Sun F, Liu J, Yang F, et al. Tetra-PEG based hydrogel sealants for *in vivo* visceral hemostasis. *Adv Mater* 2019;**31**: e1901580−90.
34. Gumpper-Fedus K, Park KH, Ma HL, Zhou XY, Bian ZH, Krishnamurthy K, et al. MG53 preserves mitochondrial integrity of cardiomyocytes during ischemia reperfusion-induced oxidative stress. *Redox Biol* 2022;**54**:102357.
35. Shao JX, Yang X, Liu TY, Zhang TT, Xie Q, Xia WL. Autophagy induction by SIRT6 is involved in oxidative stress-induced neuronal damage. *Protein Cell* 2016;**7**:281−90.
36. Kim S, Lee W, Jo H, Sonn SK, Jeong SJ, Seo S, et al. The antioxidant enzyme Peroxiredoxin-1 controls stroke-associated microglia against acute ischemic stroke. *Redox Biol* 2022;**54**:102347.
37. Zhang YC, Lee JH, Paull TT, Gehrke S, D'Alessandro A, Dou QH, et al. Mitochondrial redox sensing by the kinase ATM maintains cellular antioxidant capacity. *Sci Signal* 2018;**11**:eaaq0702.
38. Min Y, Kim MJ, Lee S, Chun E, Lee KY. Inhibition of TRAF6 ubiquitin-ligase activity by PRDX1 leads to inhibition of NFKB activation and autophagy activation. *Autophagy* 2018;**14**:1347−58.
39. Zhao Q, Ding Y, Deng ZS, Lee OY, Gao P, Chen P, et al. Natural products triptolide, celastrol, and withaferin A inhibit the chaperone activity of peroxiredoxin I. *Chem Sci* 2015;**6**:4124−30.
40. Li JW, Wang RL, Xu J, Sun KY, Jiang HM, Sun ZY, et al. Methylene blue prevents osteoarthritis progression and relieves pain in rats *via* upregulation of Nrf2/PRDX1. *Acta Pharmacol Sin* 2022;**43**:417−28.
41. Olagnier D, Lababidi RR, Hadj SB, Sze A, Liu YL, Naidu SD, et al. Activation of Nrf2 signaling augments vesicular stomatitis virus oncolysis *via* autophagy-driven suppression of antiviral immunity. *Mol Ther* 2017;**25**:1900−16.
42. Fujiki K, Inamura H, Sugaya T, Matsuoka M. Blockade of ALK4/5 signaling suppresses cadmium- and erastin-induced cell death in renal proximal tubular epithelial cells *via* distinct signaling mechanisms. *Cell Death Differ* 2019;**26**:2371−85.
43. Zheng ZG, Zhu ST, Cheng HM, Zhang X, Cheng G, Thu PM, et al. Discovery of a potent SCAP degrader that ameliorates HFD-induced obesity, hyperlipidemia and insulin resistance *via* an autophagy-independent lysosomal pathway. *Autophagy* 2021;**17**:1592−613.
44. Mu Y, Wu G, Su C, Dong Y, Zhang K, Li J, et al. pH-sensitive amphiphilic chitosan-quercetin conjugate for intracellular delivery of doxorubicin enhancement. *Carbohydr Polym* 2019;**223**:115072.
45. Wang RN, Yin CF, Liu CR, Sun Y, Xiao PP, Li J, et al. Phenylboronic acid modification augments the lysosome escape and antitumor efficacy of a cylindrical polymer brush-based prodrug. *J Am Chem Soc* 2021;**143**:20927−38.
46. Lin Q, Li S, Jiang N, Shao X, Zhang M, Jin H, et al. PINK1−parkin pathway of mitophagy protects against contrast-induced acute kidney injury *via* decreasing mitochondrial ROS and NLRP3 inflammasome activation. *Redox Biol* 2019;**26**:101254−70.
47. Fang T, Koo TY, Lee JG, Jang JY, Xu Y, Hwang JH, et al. Anti-CD45RB antibody therapy attenuates renal ischemia−reperfusion injury by inducing regulatory B cells. *J Am Soc Nephrol* 2019;**30**: 1870−85.
48. Ralto KM, Rhee EP, Parikh SM. $NAD^+$ homeostasis in renal health and disease. *Nat Rev Nephrol* 2020;**16**:99−111.
49. Bhargava P, Schnellmann RG. Mitochondrial energetics in the kidney. *Nat Rev Nephrol* 2017;**13**:629−46.
50. Berdasco C, Pinto A, Calabró V, Arenas D, Cangelosi A, Geoghegan P, et al. Shiga toxin 2 from enterohemorrhagic *Escherichia coli* induces reactive glial cells and neurovascular disarrangements including edema and lipid peroxidation in the murine brain hippocampus. *J Biomed Sci* 2019;**26**:16−38.
51. Li H, Fan C, Lu H, Feng C, He P, Yang X, et al. Protective role of berberine on ulcerative colitis through modulating enteric glial cells−intestinal epithelial cells−immune cells interactions. *Acta Pharm Sin B* 2020;**10**:447−61.
52. Hong ZX, Cao J, Liu DD, Liu MZ, Chen MY, Zeng FN, et al. Celastrol targeting Nedd4 reduces Nrf2-mediated oxidative stress in astrocytes after ischemic stroke. *J Pharm Anal* 2023;**13**:156−69.
53. Gao Y, Chu SF, Li JP, Zhang Z, Yan JQ, Wen ZL, et al. Protopanaxtriol protects against 3-nitropropionic acid-induced oxidative stress in a rat model of Huntington's disease. *Acta Pharmacol Sin* 2015;**36**:311−22.
54. Mamillapalli R, Cho S, Mutlu L, Taylor HS. Therapeutic role of uterine-derived stem cells in acute kidney injury. *Stem Cell Res Ther* 2022;**13**:107.
55. Han WK, Bailly V, Abichandani R, Thadhani R, Bonventre JV. Kidney injury molecule-1 (KIM-1): a novel biomarker for human renal proximal tubule injury. *Kidney Int* 2002;**62**:237−44.
56. Arai S, Kitada K, Yamazaki T, Takai R, Zhang X, Tsugawa Y, et al. Apoptosis inhibitor of macrophage protein enhances intraluminal debris clearance and ameliorates acute kidney injury in mice. *Nat Med* 2016;**22**:183−93.